Received: Added at production | Revised: Added at production | Accepted: Added at production

DOI: xxx/xxxx

ARTICLE TYPE

Hemodynamic effects of blood clots trapped by an inferior vena cava filter

Josep M. López*[1] | Gerard Fortuny[1] | Dolors Puigjaner[1] | Joan Herrero[2] | Francesc Marimon[3]

[1]Departament d' Enginyeria Informàtica i Matemàtiques, Universitat Rovira i Virgili. Tarragona, Catalunya, Spain

[2]Departament d' Enginyeria Química, Universitat Rovira i Virgili. Tarragona, Catalunya, Spain

[3]Departament de Medicina i Cirurgia, Universitat Rovira i Virgili, Hospital Sant Joan, Reus, Catalunya, Spain

Correspondence

*Josep M. López, Departament d' Enginyeria Informàtica i Matemàtiques, Universitat Rovira i Virgili, Av Països Catalans 26, Tarragona, Catalunya, Spain. Email: josep.m.lopez@urv.cat

Summary

The alteration of blood flow around an OPTEASE® inferior vena cava filter with one or two blood clots attached was investigated by means of computational fluid dynamics. We used a patient–specific vein wall geometry, and we generated different clot models with shapes adapted to the filter and vein wall geometries. A total of eight geometries, with one or two clots and a total clot volume of 0.5 or 1 cm^3, were considered. A non–Newtonian model for blood viscosity was adopted and the possible development of turbulence was accounted for by means of a three–equation model. Two blood flow rates were considered for each case, representative for rest and exercise conditions. In exercise conditions, flow unsteadiness and even turbulence was detected in some cases. Pressure and wall shear stress (WSS) distributions were modified in all cases. Clots attached to the filter downstream basket considerably increased averaged WSS values by up to almost 50%. In all the cases a flow recirculation region appeared downstream of the clot. The degree of flow stagnation in these regions, an indicator of propensity to thrombogenesis, was estimated in terms of mean particle residence times and mean blood viscosity. High levels of flow stagnation were detected in rest conditions in the wake of those clots that were placed upstream from the filter. Our results suggest that one downstream placed big clot, showing a higher tendency to induce flow instabilities and turbulence, might be more harmful than two small clots placed in tandem.

KEYWORDS:

Inferior vena cava filters, Computational fluid dynamics, Wall shear stress, Hemodynamics, Blood clot

1 | INTRODUCTION

Pulmonary embolism (PE) is a severe disease that can be life-threatening if left untreated. It occurs when blood flow in the pulmonary vascular system is partially blocked. In most cases, PE is caused by thrombi (blood clots) that migrate from deep veins in the legs and become lodged in the pulmonary vessels. Reports conducted in several countries in the last decade revealed that PE incidence was within the range of 0.5 – 1.1 per 1000 persons–year[1–4]. The standard treatment for PE, the administration of anticoagulant drugs[5], is complemented under certain circumstances with the implantation of a filter in the inferior vena cava (IVC)[6–8]. IVC filters are metal devices created to help in the prevention of PE by capturing thrombi that are traveling with the blood flow and could therefore reach the pulmonary vessels. The efficacy of IVC filter implantation as a therapy is disputed. A clinical study made on a large basis of 1200 patients suggested the convenience of IVC filter placement in those DVT patients with diagnosed PE[8]. On the contrary, other clinical studies concluded that the implantation of an IVC filter brings no statistically significant benefit to patients treated with anticoagulant therapy[9]. In addition, a number of possible complications following implantation of filters have been reported, such as IVC thrombosis, or filter tilting, fracture and migration[10,11]. In our previous computational fluid dynamics (CFD) simulations[12] we showed the importance of knowing the drag forces acting on the filter as high values of these forces might contribute to the appearance of the aforementioned complications.

The focus of the current study is on the alteration of the blood flow caused by the presence of one or two blood clots attached to an OPTEASE® retrievable IVC filter[13]. This particular filter model has become in recent years a popular choice among practitioners; for example, 1 787 out of a total of 13 151 entries on IVC filters in the MAUDE database[14] over the past five years corresponded to the OPTEASE® model. The OPTEASE® IVC filter displays a hexagonal symmetric double basket geometry which provides two different clot capturing areas. The topic on how the presence of an IVC filter, with clots attached to it, affects the blood flow has been the subject of a number of studies. It seems well established that partial occlusion of the vein due to the presence of clots leads to the appearance of regions with flow recirculation[15,16] or even turbulent flow[17–20]. In turn, these recirculating flow regions would be prone to become areas of thrombogenesis[16,21,22]. Harlal et al.[18] used a photometric technique to visualize the disturbance on the flow around a TRAPEASE® IVC filter (a non–retrievable precursor of the OPTEASE® filter) induced by the presence of large clots ($1.5\,\mathrm{cm}^3$) attached either to the upstream or the downstream basket. These authors reported large regions of flow stagnation and/or flow reversal, with the presence of flow unsteadiness and high–intensity turbulence, in the wake of the clots. Stewart et al.[15] performed measurements of the partially occluded flow around the TRAPEASE® IVC filter (as well as other two filter models) by means of the digital particle imaging velocimetry. In their experiments with a $1.62\,\mathrm{cm}^3$ clot upstream from the filter these authors observed the presence of flow recirculation zones both upstream and downstream of the clot.

Early *in vitro* experimental studies, such as the ones cited in the previous paragraph[15,17,18], were conducted using tubes to model the IVC wall. More recently, the availability of 3D printers has made possible the use of patient–averaged models for the vein wall[23,24]. Similarly, CFD simulations have evolved from the simple tube geometry[16] into patient–averaged models[19,20,25] and, more recently, patient–specific models[12,26] for the IVC wall. The latter computational works[12,26] showed that patient–specific vein models together with a non–Newtonian model for blood viscosity are to be used in CFD simulations when accurate predictions of WSS and secondary flow features are desired.

In the experiments and CFD simulations cited above, some basic shapes were assumed for the clot models. As an example, Wang et al.[27] produced a visual scale for clots with volumes in the $0.25 - 4\,\mathrm{cm}^3$ range modeled either as spheres or cones plus hemispheres. In particular, for clots trapped in the central part of the vein common shapes are spheres[16,20], cylinders ended with hemispheres[16] and cones (frustums) ended with one (two) hemispheres[16,17,25,26]. For clots trapped next to the vein wall, commonly considered geometries are spheres[16] and half– or full–tori, either circular or ellipsoidal[15,17,19]. Such basic shapes commonly assumed for the blood clots are not quite realistic, as shown in some instances of cavograms available in the literature[28–30]. It is observed that the clots tend to adapt to the shapes of the filter and, in the case of upstream clots, also to the vein wall. Hence, the assumption of unrealistic basic shapes for clots may become a limitation in the CFD simulations. To address this issue we propose to use clot models whose shapes are in better agreement with those observed in cavograms.

In the present work we simulated the partially occluded flow around an OPTEASE® IVC filter using a patient specific geometry for the vein with two different infrarenal blood flow rates, namely $V_{in} = 20$ and $80\ \mathrm{cm}^3/\mathrm{s}$, respectively representative of the rest and exercise conditions of the patient[12]. We designed clot models that displayed shapes completely adapted to the geometries of the filter and/or the vein wall. We set the focus on issues such as the existence of flow stagnation and flow recirculation zones and even the development of flow instabilities and turbulence. Moreover, we paid special attention to the assessment of increased WSS and pressure levels on the vein walls as a result of the presence of one or two clots attached to the filter.

2 | MODELS AND METHODS

2.1 | Geometry models

Both the patient–specific IVC geometry model and the OPTEASE® filter geometry model, pictured in Figure 1, are the same that were used in our previous work[12]. The IVC geometry was built from computed tomography (CT) images of a real patient who did not have any filter inserted. The vein segment is 14.1 cm long in the vertical (z) direction and it includes the entrance region of the two renal veins. The lumen areas at the inlet and outlet cross–sections respectively are $A_{in} = 3.7\ \mathrm{cm}^2$ and $A_{out} = 5.1\ \mathrm{cm}^2$

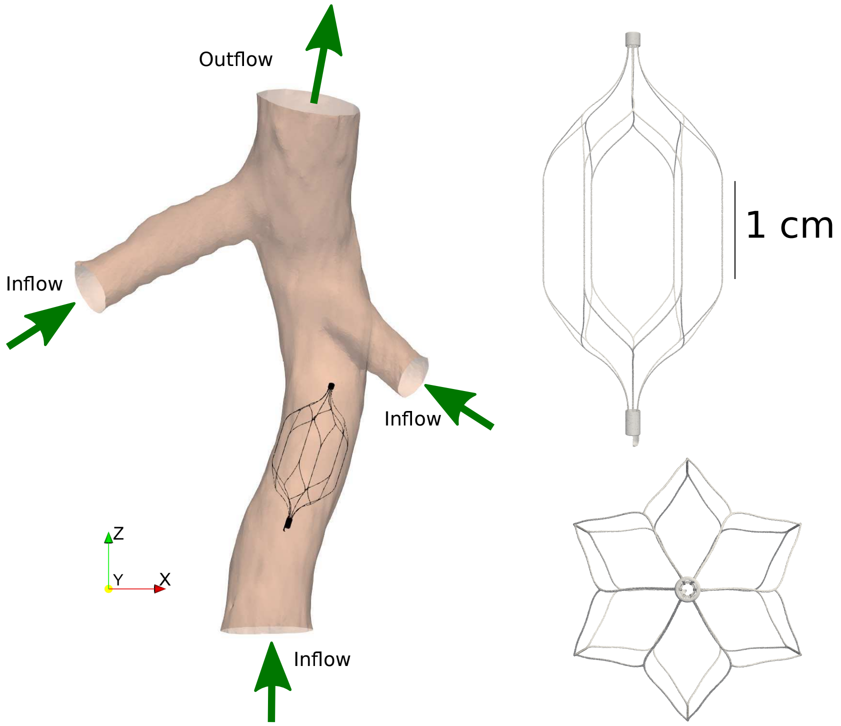

FIGURE 1 Posterior view of the IVC geometry model with the filter placed inside, together with side and zenithal projections of the filter model.

and the surface area of the vein wall is $A_{wall} = 125.3\ \mathrm{cm}^2$. The OPTEASE® filter features a double basket structure that is associated with two clot capturing regions, a lateral one upstream of the filter and a central one on the downstream basket. The surface area of the filter model is $A_{filter} = 2.703\,\mathrm{cm}^2$.

The present clot models were loosely inspired by previously published cavograms[28–30] and previous experimental and computational investigations[17–19]. Three types of clots were considered: essentially conical clots, annular clots that encircle completely a section of the vein inner wall, and piece–like clots that span only a limited angle. For each type of clot a small and a large version, having volumes close to $V_{clot} = 0.5$ and $1.0\,\mathrm{cm}^3$, respectively, were produced. Thus, six different clot models, whose geometries are shown in Figures 2 and 3, were generated. Note that the conical clots ($\mathrm{C_S}$, $\mathrm{C_L}$) are axisymmetric and are centrally placed on the downstream filter basket whereas the annular ($\mathrm{A_S}$, $\mathrm{A_L}$) and the piece–like ($\mathrm{P_S}$, $\mathrm{P_L}$) clots are asymmetric and are placed upstream from the filter (see Figure 3). The main characteristics and dimensions of these six clot models are summarized in Table 1. The premise that we followed when generating the clot models was to adapt the shape of the clot as closely as possible to the shape of the elements, filter struts and/or IVC wall, they were attached to.

Conical clots ($\mathrm{C_S}$, $\mathrm{C_L}$) were conceived as frustums with two endings shaped as a piece of an ellipsoid. As seen in Figure 4A, the frustum profiles were not modeled as straight lines but as a portion of the filter profile instead. This figure also includes the elliptic endings. Note that the connection of all pieces was required to be smooth. As a result, the conical models were thus characterized by four parameters (ζ_0, ζ_1, ζ_2, ζ_3) whose values are further constrained by the clot volume requirement. Conical clot surfaces were obtained by revolving the profile in Figure 4A around the axis of abscissas.

The generation process of both annular ($\mathrm{A_S}$, $\mathrm{A_L}$) and piece–like ($\mathrm{P_S}$, $\mathrm{P_L}$) clots comprises three steps. The first step, illustrated in Figure 4B, is the same for both types of clots and it consists in the definition of a closed curve in a plane containing the main filter axis. This curve is almost tangent to a portion of the filter and then turns to close itself beyond the vein profile. The second step is slightly different for the two kind of clots. For annular clots, a solid surface is generated by rotating the curve obtained in the first step by 360° with respect to the filter axis. In contrast, to generate piece–like clots this curve is rotated only up to some angle and during the rotation the curve is also progressively shrunk down to a point (see Figure 5A). In the third step either the annular clot or the piece–like clot is finally obtained by intersecting the surface obtained in the second step with the vein wall and keeping just the part that remains within the vein (see Figure 5B). Note that as a consequence of the realistic IVC

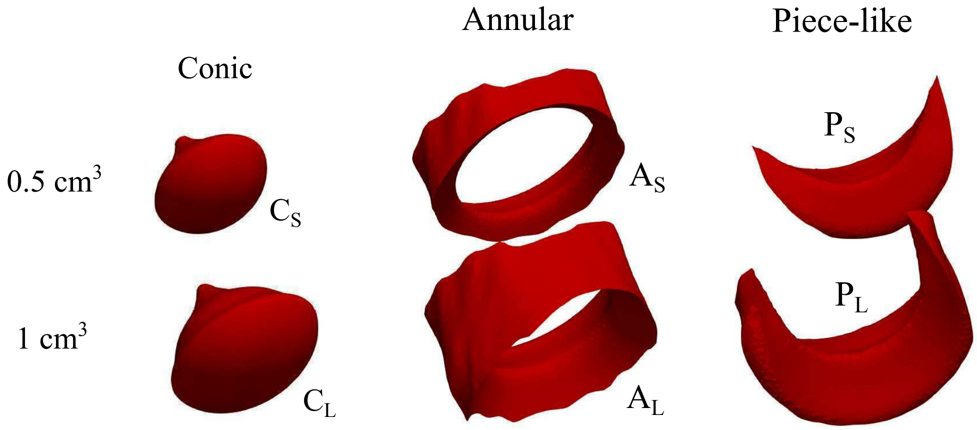

FIGURE 2 Geometry models of clots. For the sake of clarity, the size of each individual plot is not consistently scaled with the corresponding clot volume.

wall geometry the shape of the annular clot is not axisymmetric despite that the whole 360° span was revolved. Two additional geometric models were generated by combining the small downstream conical clot (C_S) with either the small annular (A_S) or the small piece–like (P_S) upstream clot. The corresponding combo models will be hereinafter referred to as C_S+A_S and C_S+P_S, respectively.

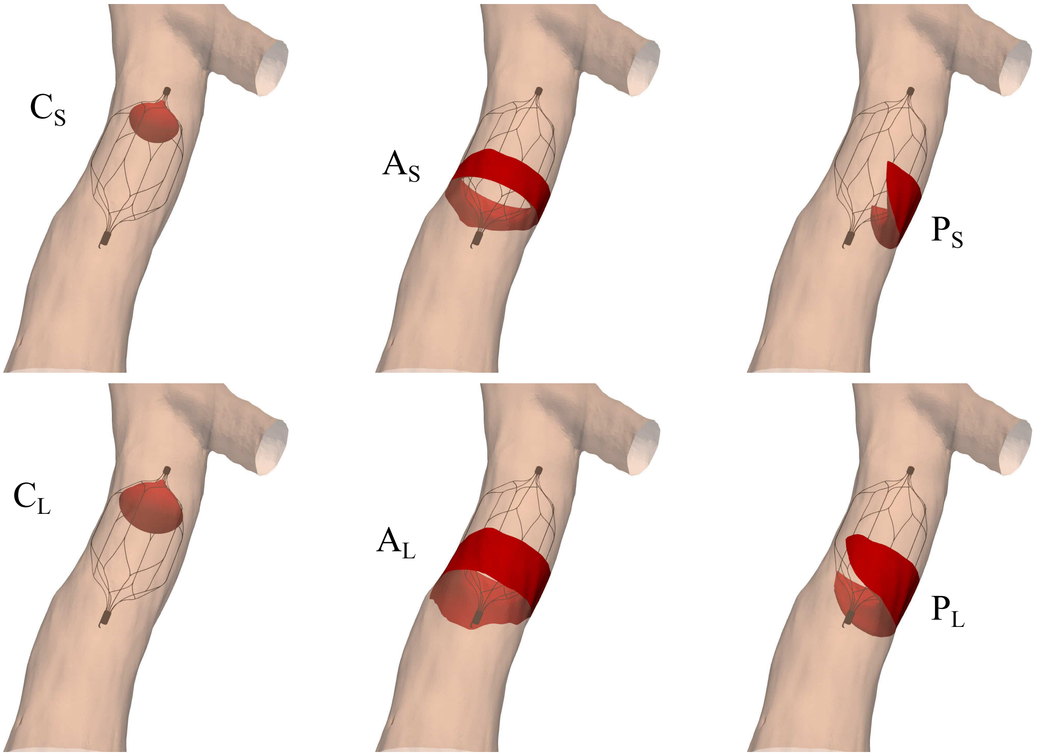

FIGURE 3 Geometric models of clots after placement in the IVC. Note that the view angle in these plots is different from the one used in Figure 2. Two additional geometries, not represented here, were generated by combining the 0.5 cm^3 conical clot with either the 0.5 cm^3 upstream annular clot (C_S+A_S) or the 0.5 cm^3 upstream piece–like clot (C_S+P_S).

Label	C_S	C_L	A_S	A_L	P_S	P_L
Brief Description	conical	conical	annular	annular	piece–like	piece–like
Volume (cm^3)	0.500	0.999	0.498	0.997	0.506	1.029
Location	Downstream basket	Downstream basket	Upstream from filter	Upstream from filter	Upstream from filter	Upstream from filter
Attached to	Filter struts	Filter struts	Filter struts & IVC wall	Filter struts & IVC wall	Filter struts & IVC wall	Filter struts & IVC wall
Axisymmetric? / Angular span	Yes / 360°	Yes / 360°	No / 360°	No / 360°	No / 164°	No / 259°
Characteristic size (cm)	1.15	1.48	0.32	0.43	0.46	0.56
Maximal length (cm)	1.00	0.78	1.15	1.24	1.34	1.25
Clot–lumen contact area (cm^2)	3.22	5.15	4.66	6.75	2.94	5.01
Clot–IVC wall contact area (cm^2)	–	–	4.14	6.99	2.64	4.44
Minimal lumen cross–area (cm^2)	2.46	1.70	2.03	1.69	2.70	2.09
Maximal vascular occlusion (%)	29.7	50.1	39.6	49.5	19.8	40.2
Number of triangles in surface mesh	4 110	24 794	8 218	11 729	4 849	8 245

TABLE 1 Main characteristics and dimensions of the clot geometry models used in the present simulations. Characteristic size stands for diameter in the conical clots (C_S, C_L) and for maximal radial protrusion length in the rest of clots.

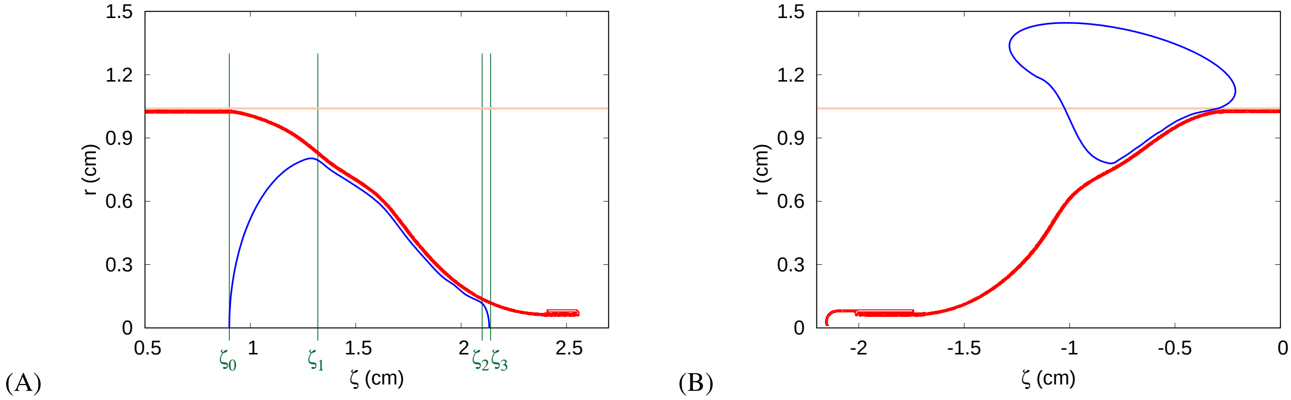

FIGURE 4 Filter (red) and clot (blue) profiles. The pale brown line, included as a reference, indicates the approximate location of the vein wall. Abscissas (ζ) correspond to length along the filter axis and ordinates (r) are radial distances to the filter axis. (A) Conical clot profile: the portion between ζ_1 and ζ_2 corresponds to the frustum and the $\zeta_0 - \zeta_1$ and $\zeta_2 - \zeta_3$ portions correspond to the ellipsoidal endings. (B) Annular and piece–like clots. The blue line represents the closed curve needed in the first step of the clot generation process. A part of it comes from the filter profile and the rest is obtained from interpolation after a few control points are customarily placed above and to the left of the filter (even outside the vein wall).

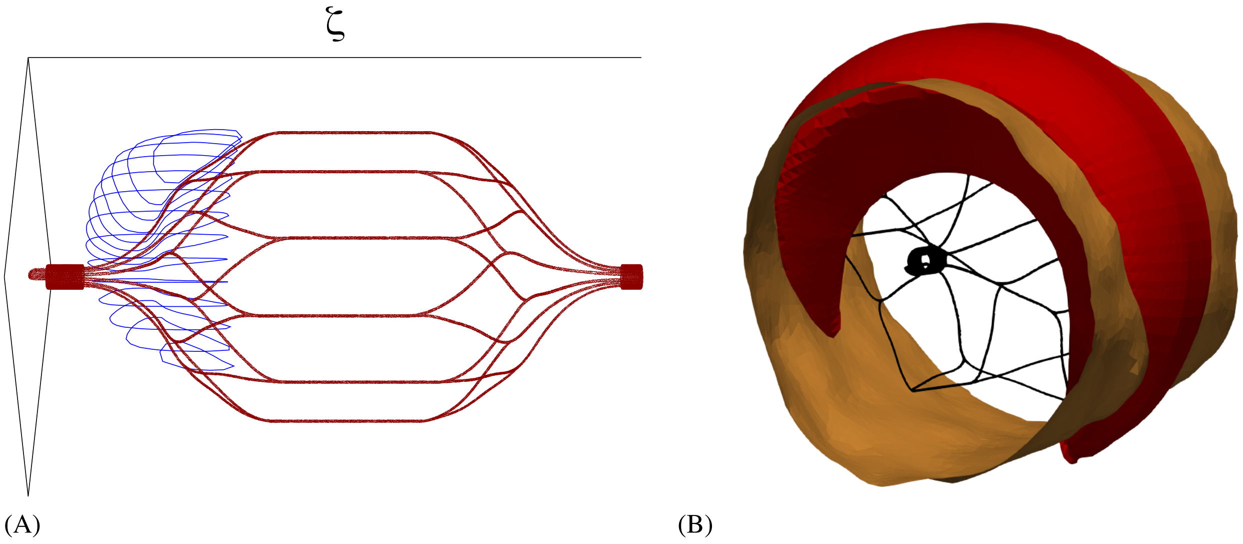

FIGURE 5 Generation of the piece–like clot models. (A) Progressive shrinking of the initial curve during the rotation process. (B) Surface of the clot (red) wrapped around the vein wall (brown). The part of the clot that is outside the vein wall is discarded.

2.2 | Computational meshes

The surface meshes for the IVC wall were obtained by means of a refinement of the same base surface mesh that was used in our previous work[12]. This base surface mesh, which was previously adopted after careful testing as the best compromise between accuracy and economy, consisted of 68 432 triangles with an average area of 0.183 mm^2 and edge lengths in the 0.55–0.8 mm range. We also showed in our previous work[12] how this base surface mesh had to be locally refined (to a maximum of 72 098 triangles) to allow a proper characterization of the flow regions around filter elements located near the IVC wall. Similarly, as illustrated in Figure 6A for the P_L case, in the present work the IVC wall meshes were specifically refined to ensure that the rich flow dynamics in the clot wake was properly captured. The edges of the triangles in the refined regions of the mesh were in the 0.25–0.4 mm range; see Figure 6B for a close–up of a region including refined and unrefined triangles. As a result of the refinement, the size of the refined IVC surface mesh was increased up to a maximum value of 104 973 triangles.

As discussed above, the annular and piece–like clots were meant to be attached to the vein wall. Consequently, a seamless connectivity between the clot and the IVC wall surface meshes was adopted in each case; a detail of such a smooth mesh connection is shown in Figure 6C for the P_L case. As is illustrated in this figure, a consistent average size of the triangles was prescribed for both the refined regions of the IVC wall mesh and the clot surface mesh. The number of triangles used in the surface meshes of each of the six clot models are included in Table 1. A unique surface mesh for the filter model, consisting of 57 270 triangles[12], was used in all the cases investigated.

Once the surface meshes for the IVC wall, filter and clot models were created and properly combined for each of the geometries considered, the corresponding three–dimensional (3D) meshes to be used in the CFD simulations were generated. These 3D meshes were based on tetrahedrons with the total number of cells ranging between 4 073 828 and 10 315 813, the highest number corresponding to the case with the large piece–like clot (P_L). The general trend was that relatively large 3D meshes were needed in those cases with an upstream clot due to the refinement introduced in the IVC wall surface mesh (see Figure 6) and also to the fact that annular and, especially, piece–like clots, protrude into the vein lumen (see the characteristic size entry in Table 1). The use of large 3D meshes increases the computational cost of the CFD simulations but this is a price worth paying considering that long flow recirculation regions, featuring rich dynamics, are to be expected in the clot wake[15,17,18].

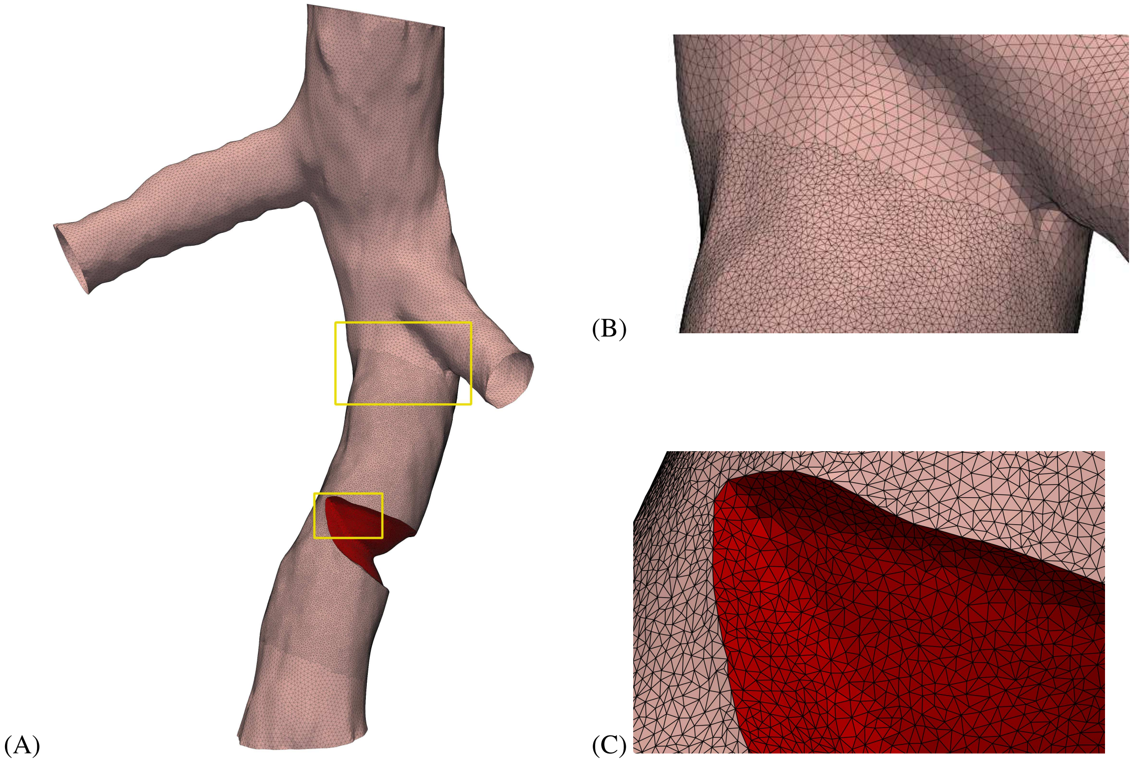

FIGURE 6 Example of triangular mesh on vein (pink) and clot (red) walls. (A) General view for the P_L case with a vein wall mesh refined in the area near clot and filter. Rectangles correspond to areas magnified in (B) and (C). (B) Detail of an area in the vein wall mesh with refined and unrefined parts. (C) Detail of an area including vein and inner clot walls.

2.3 | Conservation equations

The CFD simulations were performed using the OpenFOAM open source code[31]. The code solves numerically the differential mass and momentum conservation equations for an incompressible flow,

$$\frac{\partial U}{\partial t} + (U \cdot \nabla) U = -\frac{1}{\rho}\nabla p + \left\{ \nabla \cdot \left[\left(\frac{\mu + \mu_T}{\rho} \right) \nabla \right] \right\} U \qquad (1)$$

$$\nabla \cdot U = 0 \qquad (2)$$

where $U = (u_x, u_y, u_z)$ is the velocity vector, p is the dynamic pressure, ρ is the fluid density, μ is the fluid molecular viscosity and $\mu_T/\rho = \nu_T$ is the so called turbulent or eddy kinematic viscosity which accounts for the possible effects of turbulence on the mean flow field. Equations (1) and (2) were solved under the no–slip boundary conditions ($u_x = u_y = u_z = 0$) at all solid walls (IVC wall, filter and clot surfaces) and a convective boundary condition with $p = 0$ was prescribed at the IVC outlet section. At the IVC and renal veins inlet sections the fully developed flow assumption was used to calculate the velocity distributions and pressure gradients[12]. A value of $\rho = 1060\,\mathrm{kg/m^3}$ was used for the blood density and the non–Newtonian Bird–Carreau viscosity model[32],

$$\mu = \mu(\gamma) = \mu_\infty + (\mu_0 - \mu_\infty)[1 + (\lambda\gamma)^2]^{(n-1)/2} \qquad (3)$$

was assumed. In Eq. 3, the values of the constants were $\lambda = 3.313$ s, $n = 0.3568$, $\mu_\infty = 3.45\times10^{-3}$ Pa · s and $\mu_0 = 0.056$ Pa·s[33], and the scalar quantity γ is the so–called shear rate, which depends on the second invariant (II) of the rate–of–strain tensor, $\boldsymbol{\gamma}$:

$$\gamma = \sqrt{\frac{1}{2}II} = \sqrt{\frac{1}{2}\sum_i \sum_j \gamma_{ij}\gamma_{ji}} \quad ; \quad \gamma_{ij} = \left(\frac{\partial u_i}{\partial x_j} + \frac{\partial u_j}{\partial x_i} \right) \quad ; \quad i,j = 1,2,3 \qquad (4)$$

The use of a non–Newtonian viscosity model for blood in the CFD simulations has been recommended as it provides a more reliable description of the blood flow in the IVC[12,26]. The Bird–Carreau model, which was also used in our previous work[12], has become a popular choice for modeling blood flow[26,34–41]. It should be however noted that many other non–Newtonian models have also been used quite often in previous studies to characterize blood viscosity; see, for example[35,37–42].

For the eddy viscosity, ν_T, we used the $k_L - k_T - \omega$ closure model of Walters and Cokljat[43],

$$\nu_T = \nu_T(k_L, k_T, \omega) \tag{5}$$

where k_L and k_T respectively are the laminar and turbulent specific kinetic energy and ω is interpreted as an inverse time–scale for turbulence. In the $k_L - k_T - \omega$ model an additional partial differential equation for each of these three turbulent quantities must be solved together with Eqs. (1) and (2)[43] (these differential equations are not included here for the sake of conciseness). Wrankat and Cokljat's model was devised to predict transitional flows and it is therefore suitable to the present problem where the blood flow, originally laminar, might endeavor transition to turbulence due to the disturbance imposed by the presence of clots. In fact, Ren et al.[20], who used the $k_L - k_T - \omega$ model in the simulation of Newtonian blood flow with an idealized vein and clot geometry, observed the development of high levels of turbulent kinetic energy downstream of the obstacle in some instances. The present setup of the turbulence simulation differs from Ren et al.'s in one relevant aspect. Ren et al. prescribed significant levels of turbulence in all the inlet streams whereas we instead imposed the condition

$$k_L = k_T = \nu_T = 0 \tag{6}$$

at the three inlet sections. That is, all blood flows entering the IVC segment were assumed to be fully laminar so that turbulence, if actually developed, would be exclusively the result of internal flow instabilities.

In our previous work[12] we solved the conservation equations for steady state solutions only, that is, we assumed $\partial U/\partial t = 0$ in Eq. (1). Since one of the aims of the present study is to investigate flow unsteadiness we also solved the conservation equations (including the ones for k_L, k_T and ω) using the Euler first order implicit time–marching scheme. In these unsteady flow simulations, the inlet velocity and pressure boundary conditions were held at constant (time–independent) values, an approach referred to by Ren et al.[20] as *statistically stationary* flow conditions. The initial conditions $U(t = 0) = k_L(t = 0) = k_T(t = 0) = \omega(t = 0) = 0$ were imposed on all the calculation cells. Numerical testing proved that a uniform time step of $\Delta t = 10^{-3}$ s was small enough to guarantee the accuracy and stability of the time–marching procedure. Since the complete time–integration procedure was found to be far more computationally expensive than it was the corresponding steady flow simulation (typically, about one order of magnitude in terms of total CPU time), we first carried out steady state simulations for all the cases considered and only in those cases where convergence into a stationary solution was not achieved the corresponding unsteady simulation was launched. In all of such instances, the solution was found to evolve into a periodic orbit and after time–periodicity was well established (no significant changes on oscillation amplitude and frequency were observed) time–integration was maintained for at least ten additional cycles. Hence, we assumed that only one stable solution of the conservation equations, either a steady state or a time–periodic one, exists for each of the cases considered. To test such a hypothesis, we slightly perturbed all the previously obtained solutions and used the perturbed field as the initial condition for the corresponding unsteady flow simulation; in all the cases, the disturbance decayed very fast and the time–marching sequence was therefore promptly returning into the original solution.

2.4 | Post–processing

The open–source Paraview software[44] was used for the visualization of the calculated flow solutions (a specifically tailored version of Paraview is included by default in the standard OpenFOAM installation). As will be seen in what follows, we used Paraview to plot contours of wall shear stress and pressure on solid–surfaces, to plot contours of different quantities on certain slices of the lumen volume, to integrate and plot flow streamlines and to determine and plot the shape of 3D iso–surfaces while determining altogether the resulting enclosed volume.

We used the OpenFOAM built–in post–processing utility to compute the wall shear stress (WSS) distributions on the solid surfaces and their surface averaged values ($\overline{\text{WSS}}$). The resultant skin friction force ($\vec{F}_f$) over the whole surface was computed by numerical integration of the local values available on each cell. The resultant surface averaged pressure force ($\vec{F}_p$) vector was computed in a similar way but taking into account that local forces exerted by pressure are normal to each particular surface cell. The corresponding moduli of these resultant forces are respectively denoted as F_f and F_p. The resultant drag force, i.e., the overall drag exerted by the blood flow on a given surface, was then calculated as $\vec{F}_d = \vec{F}_f + \vec{F}_p$ and its modulus is denoted as F_d. One may expect the total viscous force, F_f, on a given surface element to be roughly proportional to the element surface area while the total pressure force, F_p, would be also dependent on the particular orientation of the surface element; that is, surface elements transversely aligned to the blood flow may yield considerably high F_p values[12]. Note that $F_d = |\vec{F}_f + \vec{F}_p| \leq F_f + F_p$ due to

$$F_d^2 = \left(F_f + F_p\right)^2 - 2F_f F_p (1 - \cos\theta) \tag{7}$$

where θ denotes the angle between the $\vec{F}_f$ and $\vec{F}_p$ vectors. That is, F_d will be smaller than the sum of F_f and F_p unless the viscous and pressure force vectors are perfectly aligned ($\theta = 0$).

In the unsteady flow simulations, a number of instantaneous fields were stored on disk during the time–integration. Surface averaged wall shear stress and resultant forces were calculated for each of these instantaneous fields and finally the time–average of each quantity was computed. It is interesting that even though large oscillations in time of local quantities were detected (as will be shown below) the variations in time of surface average quantities ($\overline{\mathrm{WSS}}$, F_f, F_p) were small (instantaneous values of these quantities departed at most about a 0.5% from the time–averaged value). As an indicator of the potential development of turbulence, we monitored the turbulence intensity, T_U, based on the so–called total fluctuation kinetic energy[43] ($k_L + k_T$) and the modulus of local velocity ($|U|$):

$$T_U = 100\frac{\sqrt{2\left(k_L + k_T\right)}}{|U|} \tag{8}$$

3 | RESULTS

Two different values of the inlet blood flow rate, respectively representative of the rest and exercise conditions of the patient[12], were considered at the IVC infrarenal inlet section, V_{in}, and at the two renal vein inlet sections, V_{ren}. These flow values were $V_{in} = 20$ cm^3/s (1.2 L/min) and $V_{ren} = 7$ cm^3/s (0.42 L/min) for the rest condition and $V_{in} = 80$ cm^3/s (4.8 L/min) and $V_{ren} = 10$ cm^3/s (0.6 L/min) for the exercise condition. The values of the Reynolds number at the infrarenal inlet section (based on the hydraulic diameter and surface averaged values of velocity and blood kinematic viscosity) were $Re_{in} = 141$ and 870 for the rest and exercise conditions, respectively. Steady state solutions were obtained in all the CFD simulations with the lower blood flow rates (rest condition). For the exercise condition, steady solutions were obtained in the $\mathrm{C_S}$, $\mathrm{A_S}$, $\mathrm{P_S}$, $\mathrm{A_L}$ and $\mathrm{C_S}$+$\mathrm{P_S}$ cases whereas periodic flow solutions were obtained in the $\mathrm{C_L}$, $\mathrm{P_L}$ and $\mathrm{C_S}$+$\mathrm{A_S}$ cases.

3.1 | Wall shear stress

In our previous work[12] we found that the implantation of IVC filters produced no significant change in the WSS distribution on the vein wall. As illustrated in Figure 7 for the simulations under rest conditions, the presence of blood clots attached to the OPTEASE® filter clearly alters the WSS wall distributions with a distinct contour pattern for every particular case. Conical clots (Figures 7B and 7E) produce a high WSS region downstream of the clot location. As these clots are centrally placed, the blood flow is channeled towards the vein wall. This effect leads to high velocity gradients near the wall, which in turn result in high WSS values. Annular (Figures 7C and 7F) and piece–like (Figures 7D and 7G) clots produce instead a region of low WSS downstream of the clot. As clots of these two types are attached to the vein wall, the blood flow is directed inwards thus resulting in low WSS values on the vein wall. The WSS contour plots in Figures 7H and 7I reveal that in the cases with two clots the superposition principle cannot be assumed. If we compare either Figure 7H ($\mathrm{C_S} + \mathrm{A_S}$) with Figure 7C ($\mathrm{A_S}$) or Figure 7I ($\mathrm{C_S} + \mathrm{P_S}$) with Figure 7D ($\mathrm{P_S}$) we see that the low WSS wall region past the upstream clot is considerably shorter in the combo cases ($\mathrm{C_S} + \mathrm{A_S}$, $\mathrm{C_S} + \mathrm{P_S}$). As will be seen below, the presence of a clot generates a region of flow recirculation past the obstacle. Thus, in the combo cases we may infer that the axial distance between the upstream and the downstream (conical) clots is far too short for a complete flow redevelopment.

The calculated values of surface averaged WSS on the vein wall ($\overline{\mathrm{WSS}}$) are shown in Figure 8. When compared with the filter alone case, conical clots are the ones producing the largest $\overline{\mathrm{WSS}}$ increase, especially in the $\mathrm{C_L}$ case under exercise conditions where the $\overline{\mathrm{WSS}}$ increment is almost 50%. Note that this conical clot, having a volume of 1 cm^3, largely obstructs the blood flow as it induces a maximum vascular occlusion slightly above 50% (see Table 1). As shown in Figure 9B, when compared with the filter alone case under exercise conditions (Figure 9A) the $\mathrm{C_L}$ clot not only induces the high WSS region around the clot location but a patch of high WSS also appears in the vein wall region above the right renal vein (note that highest contour level in the plot, WSS = 5 Pa, is almost four times larger than the $\overline{\mathrm{WSS}} = 1.31$ Pa reference value of the filter alone case). On the other hand, the presence of annular clots ($\mathrm{A_S}$, $\mathrm{A_L}$) produces instead a reduction in $\overline{\mathrm{WSS}}$ levels in Figure 8, a decrease which is qualitatively consistent with the corresponding local WSS wall distributions portrayed in Figures 7C and 7F. We also can see in

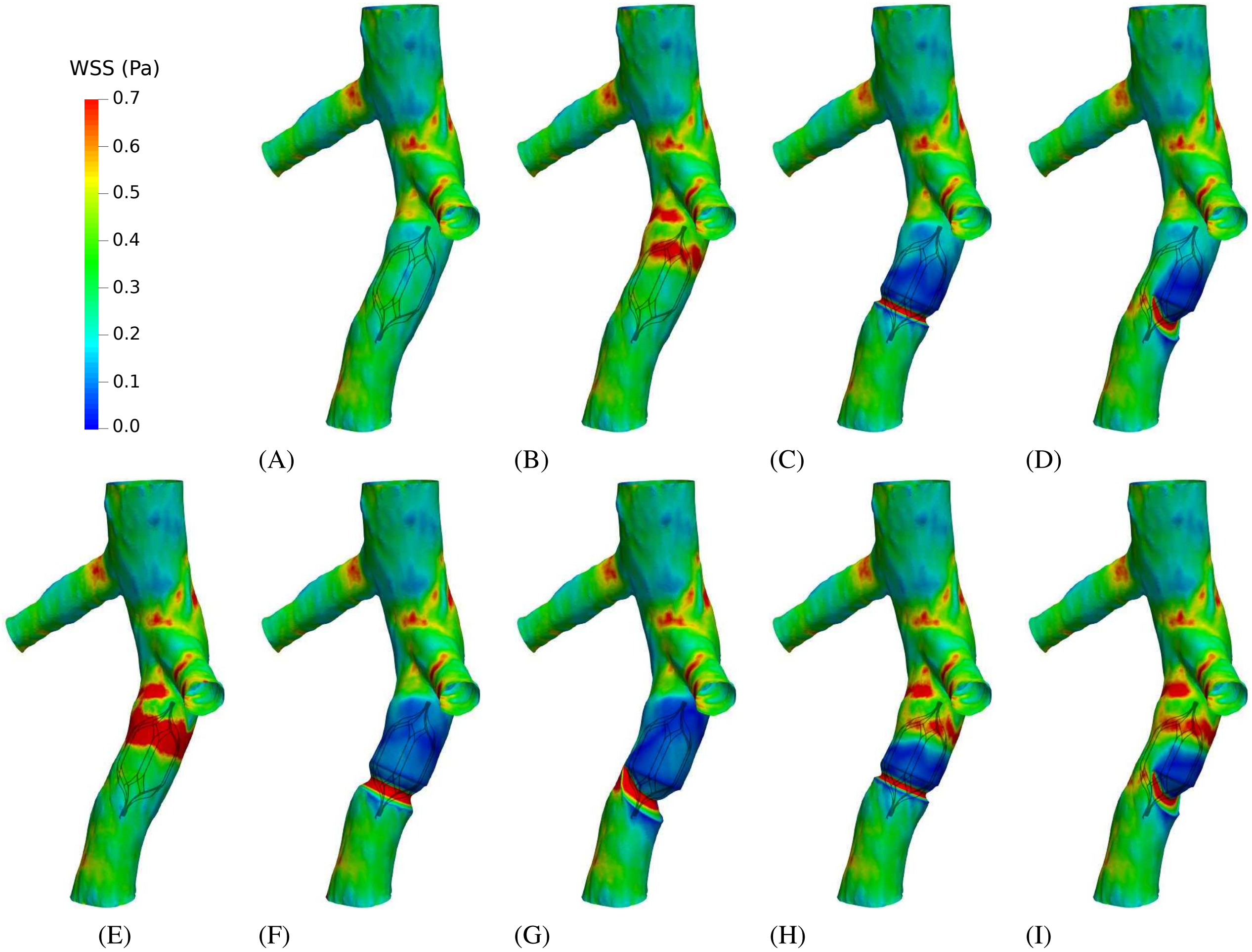

FIGURE 7 Wall shear stress (WSS) distribution on the vein wall and inner surface of annular and piece–like clots under rest conditions: (A) filter alone, (B) C_S. (C) A_S. (D) P_S. (E) C_L. (F) A_L. (G) P_L. (H) C_S+A_S. (I) C_S+P_S. See Figures 2 and 3 for the meaning of the case labels and Table 1 for a summary of each clot characteristic features.

Figure 8 that the presence of a piece–like clot (P_S, P_L) produces little change on the calculated $\overline{\text{WSS}}$ levels except for the P_L case under exercise conditions, where a significant increase of about 15% is observed. The corresponding local WSS contours plotted in Figures 9C and 9D help to qualitatively explain such an increase. As was previously observed under rest conditions (Figure 7G), a wall region of low WSS is clearly visible in Figure 9C downstream of the clot, a fact that would hint not to an increase but to a decrease of the surface averaged WSS value. As can be seen in Table 1, the P_L clot features a maximum vascular occlusion of 40.2% and its angular span is 259°. Consequently, in the P_L case under exercise conditions as the blood flow is diverted away from the side of the IVC wall the clot is attached to, it is also pushed against the opposite side of the wall. As a result, the region of high local WSS on the vein wall, shown in Figure 9D, appears. This high WSS region together with the high WSS patch above the right renal vein, also apparent in Figure 9C, more than compensate for the low WSS region downstream of the P_L clot.

High WSS values at the vein wall might be indicative of a potentially harmful situation. In particular, shear stress–mediated activation of platelets, a precursory mechanism of thrombogenesis, has been reported for sustained values of WSS above 5 Pa[45–47]. From a broader standpoint, it seems that episodes of hypertension together with high WSS values might trigger structural changes of the vein wall involving the activation of endothelial and smooth muscle cells[48].

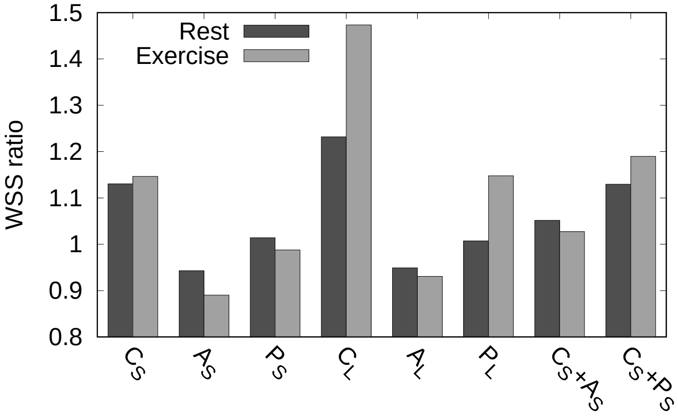

FIGURE 8 Ratio of calculated $\overline{\text{WSS}}$ values on the vein wall to the corresponding values for the filter alone case under rest and exercise conditions. The reference values in the filter alone case are $\overline{\text{WSS}} = 0.299$ and 1.310 Pa for rest and exercise conditions, respectively[12].

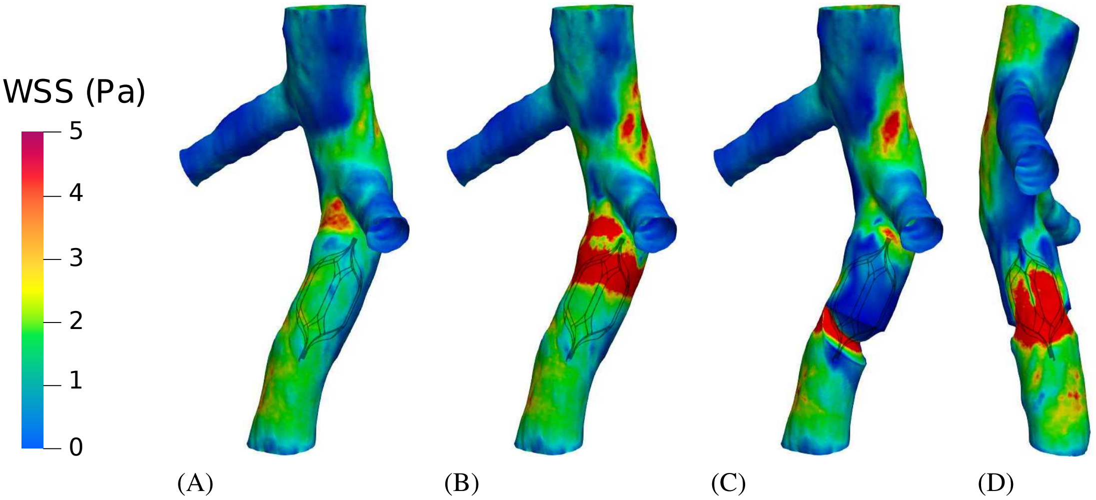

FIGURE 9 Wall shear stress (WSS) distribution on the vein wall and inner surface of the P_L clot in selected cases under exercise conditions: (A) Filter alone, no clot. (B) C_L. (C, D) P_L. In parts A–C the view angle is the same as it was in Figure 7 whereas in the plot of part D a rotation of about 140° around the z–axis was applied.

3.2 | Changes in pressure distribution

We previously found[12] that the insertion of the OPTEASE® filter resulted in an increase of the total pressure drop along the IVC segment from 4.6 to 10.7 Pa (0.080 mm Hg) in rest conditions and from 17.9 Pa to 52.8 Pa (0.40 mm Hg) in exercise conditions. Considering that the filters are designed to disturb the blood flow as little as possible, it seems that the presence of clots will notably increase the total pressure drop. Figure 10A shows the pressure distribution on the vein wall for the filter alone case and exercise conditions. This pressure distribution is taken as the reference in parts B–D where the calculated pressure variations (Δp) with respect to the filter alone case are plotted. In all the cases investigated the presence of a clot induces the appearance of a flow recirculation region past the obstacle. Such flow regions are characterized by small pressure values, as reflected by the blue regions of highly negative Δp at the vein wall in Figures 10B–D. Upstream from the obstacle pressure levels in the vein lumen experience instead a strong increase, which is reflected by the red regions of high Δp in the vein wall plots. Summary information on pressure variations for the rest of cases, not plotted in Figure 10, is given in Table 2. As a general trend, the conical clots are the ones producing the highest upstream positive variations in pressure (Δp_{99}) on the vein wall whereas the

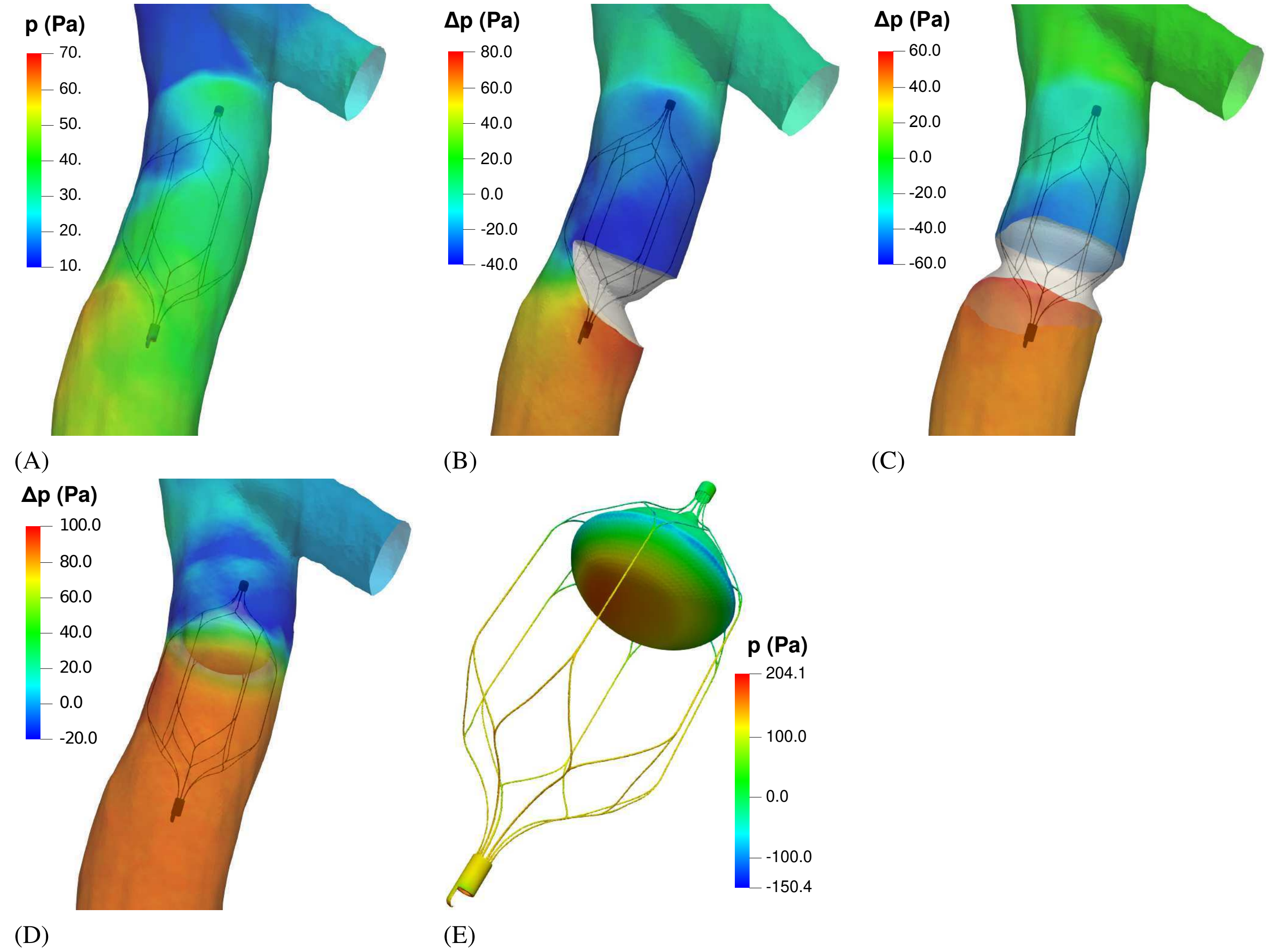

FIGURE 10 (A) Pressure distribution on the vein wall as calculated in exercise conditions for the filter alone case. Variation of pressure on the vein wall, Δp, caused by the presence of the clot for the cases (B) $\mathrm{P_L}$, (C) $\mathrm{A_L}$ and (D) $\mathrm{C_L}$. (E) Pressure distribution on the conical clot surface calculated for exercise conditions in the $\mathrm{C_L}$ case.

strongest downstream negative variations in pressure (Δp_1) correspond to the annular clots. Note that in the combo cases the values of the upstream Δp_{99} are consistent with, but slightly inferior to, the addition of the corresponding pressure variations in the single clot simulations.

It will be shown in the next subsection (3.3) that strong pressure differences along the surface of a clot will result in strong total drag forces (F_d) on the clot. As illustrated in Figure 10E for the $\mathrm{C_L}$ case under exercise conditions, pressure drops around a clot are much steeper than are pressure drops on the vein wall ($\Delta p_{99\%} - \Delta p_{1\%}$ in Table 2). The pressure contours in Figure 10E show that as the clot is being pushed by the blood flow a strong pressure rise is observed on its upstream facing elliptic–like surface, with pressure values as high as $p = 204$ Pa (1.53 mm Hg). The minimum pressure values ($p = -150$ Pa) are observed instead around the clot rim, the imaginary line where the clot reaches its maximal diameter. The blue colored ring with very low (negative) p values denotes that flow separation occurs at the clot rim, a physical phenomenon which in turn originates the flow recirculation phenomena that will be analyzed in subsection 3.4. In addition, variations in the pressure around a clot are also important because they suggest that the clot is experiencing strong forces. The analysis of the forces is the topic of the next section.

		C_S	A_S	P_S	C_L	A_L	P_L	C_S+A_S	C_S+P_S
Rest	$\Delta p_{99\%}$ (Pa)	3.71	1.79	1.12	9.07	3.49	4.27	5.09	4.58
	$\Delta p_{1\%}$ (Pa)	−0.40	−2.36	−1.07	−1.67	−3.73	−3.52	−0.60	−0.39
	$\Delta p_{99\%} - \Delta p_{1\%}$ (Pa)	4.11	4.15	2.19	10.74	7.22	7.79	5.69	4.97
Exercise	$\Delta p_{99\%}$ (Pa)	26.4	27.5	14.2	91.7	49.0	67.9	51.0	38.6
	$\Delta p_{1\%}$ (Pa)	−8.9	−36.2	−16.8	−27.8	−44.3	−37.9	−15.3	−10.0
	$\Delta p_{99\%} - \Delta p_{1\%}$ (Pa)	35.3	63.7	31.0	119.5	93.3	105.8	66.3	48.6

TABLE 2 Statistically significant values of pressure variations on the vein wall (Δp, or pressure in the filter plus clot case minus pressure in the filter alone case). A value of $\Delta p_{1\%}$ means that 1% of the vein wall surface has this value of Δp or less. A value of $\Delta p_{99\%}$ means that 1% of the vein wall surface has this value of Δp or more. $\Delta p_{99\%}$ and $\Delta p_{1\%}$ indicate the maximal and minimal values of the variation of pressures between each case and the filter alone case. The values $\Delta p_{99\%} - \Delta p_{1\%}$ provide an estimate of the pressure drop around the clot.

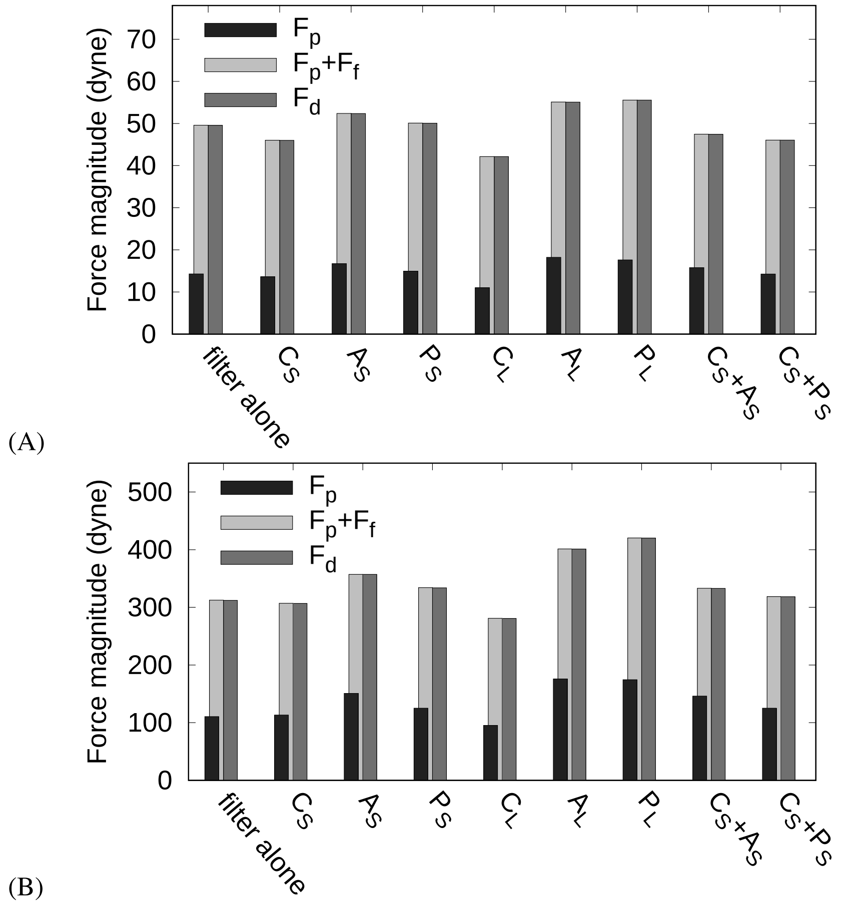

FIGURE 11 Magnitude of the pressure (F_p), pressure plus skin friction ($F_p + F_f$) and total drag (F_d) forces exerted on the filter surface under (A) rest conditions and (B) exercise conditions.

3.3 | Forces on the filter and clot surfaces

In our previous work[12] we found that, in the absence of a clot, the magnitude of the surface averaged total drag force on the OPTEASE® filter was about $F_d = 50$ and 300 dyne under rest and exercise conditions, respectively. Figure 11 shows the values of the total forces on the filter calculated in each of the simulations. The leftmost column of these plots corresponds to the filter alone case. The presence of clots provokes a change in the values of both the skin friction (F_f) and pressure (F_p) forces exerted on the filter. It is noticeable that, as a general rule, the total drag force (F_d) exerted on the filter is increased when annular or piece–like clots are present whereas it is reduced if there is a conical clot instead. Figure 12 shows that the F_d values on the surface of a clot are much larger than the corresponding values on the filter surface in Figure 11. We can also see in Figure 12 that in all the cases F_p is much larger than F_f. Comparison of Figure 12A with Figure 12B shows that a four fold increase in the infrarenal blood flow rate, from rest to exercise conditions, leads in most cases to an increase of about one order of magnitude in the clot F_d values. In rest conditions (Figure 12A) the small piece–like clot $\mathrm{P_S}$ produces a total drag force, F_d, larger than do the other two small clots ($\mathrm{A_S}$ and $\mathrm{C_S}$) despite having smaller clot–lumen contact area (see Table 1). Figure 12A also shows that $F_d < F_f + F_p$ for the cases with a piece–like clot ($\mathrm{P_S}$, $\mathrm{C_S}$+$\mathrm{P_S}$). The reason for the inequality is that the two resultant force vectors, $\vec{F}_p$ and $\vec{F}_f$, are not well aligned ($\theta \gg 0$ in Eq. (7)). The pressure force ($\vec{F}_p$) in the piece–like clots is roughly aligned normal to the IVC wall whereas in the conical and annular clots $\vec{F}_p$ is well aligned with the blood flow direction (more or less oriented along the $z-$axis). The conical and annular clots are axisymmetric (or nearly so) and therefore a large amount of cancellation between the $x-$ and $y-$ components of the local $\vec{F}_p$ takes place during the surface integration. The comparatively short angular span of the $\mathrm{P_S}$ clot (156 °; see Table 1) precludes most of the cancellation effect and the resulting angle between $\vec{F}_p$ and the main flow direction is about 80 °. This alignment of $\vec{F}_p$ in the $\mathrm{P_S}$ case reflects the fact that the blood flow is pushing the piece–like

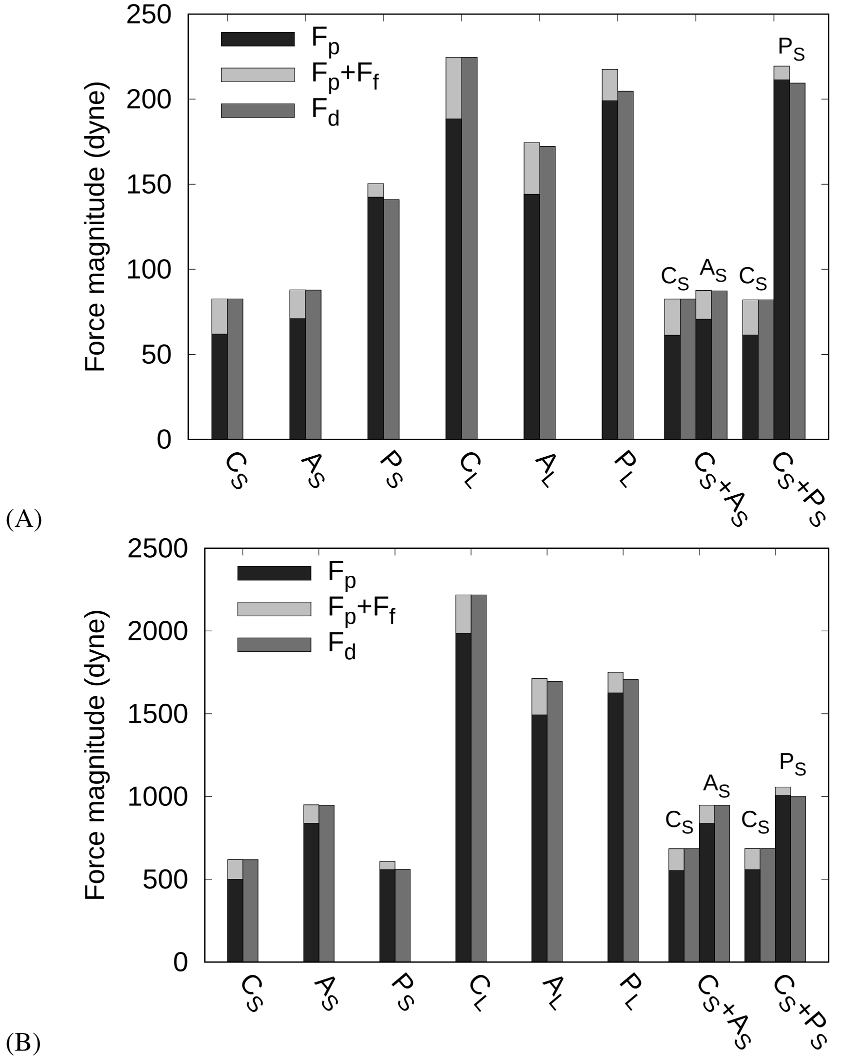

FIGURE 12 Magnitude of the forces on the surface of the clots under (A) rest conditions (B) exercise conditions. For the sake of clarity, columns for F_p and $F_p + F_f$ are superimposed.

clot mostly against the vein wall. The largest P_L clot is at an intermediate position: with a larger angular span of 259 ° the angle between $\vec{F}_p$ and the main flow direction is about 60 °. Note that in the C_S+P_S combo case, the contribution to F_d from the P_S element is considerably larger than the corresponding F_d value for the piece–like clot case, P_S, (see Figure 12).

A question related to the above discussion is what fraction of the F_d force on annular and piece–like clots is supported by the filter, or otherwise is directly supported by the vein wall region the clot is attached to. The aforementioned results on the $\vec{F}_p$ alignment suggest that in the smaller piece–like clot (P_S) most of the total drag force will be sustained by the vein wall tissue surrounding the clot. With conical clots, and to a lesser extent with annular clots, the drag force exerted by the blood flow on the clot would be in turn transferred from the clot into the filter. The F_d values plotted in Figures 11 and 12 therefore suggest that as a result of having trapped one or more clots the total force exerted by the filter on the vein wall at its docking sites might become several times larger. Consequently, the risk of complications such as filter tilting, migration or strut fractures would be also considerably higher, especially under exercise conditions.

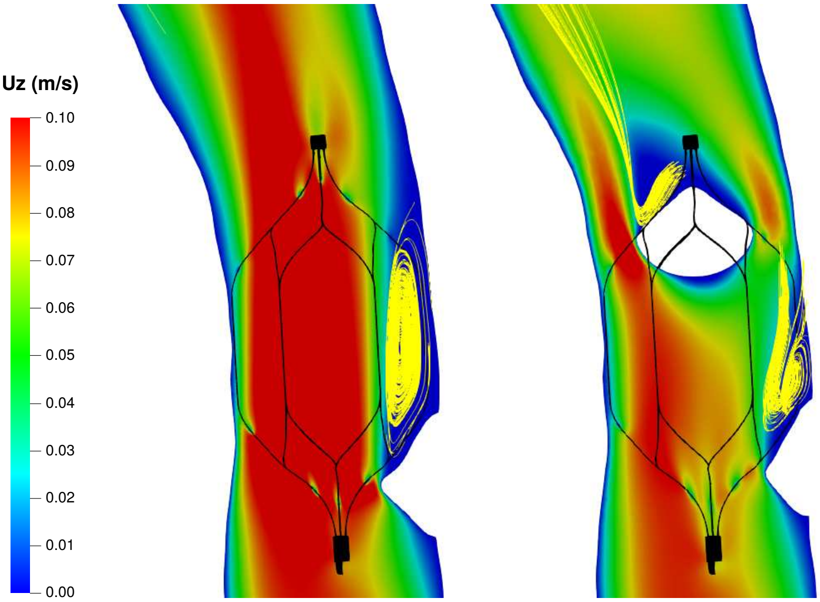

(A) (B)

FIGURE 13 Contour plots of the vertical velocity component, U_z, at a selected plane slice for the (A) P_L and (B) C_S+P_S simulations under rest conditions. Projections of a number of 3D streamlines, originated downstream of the clots, are also shown. The slice plane has been chosen to contain the filter axis and to divide the piece–like clot into two roughly symmetric parts. The final integration time was the same for all the particle trajectories plotted.

3.4 | Flow recirculation regions

Flow recirculation regions are formed downstream of the clot in all the cases considered, as respectively illustrated in Figure 13A and B for the P_L and C_S+P_S cases under rest conditions. In those cases with annular or piece–like clots alone, the blood flow is channeled through the central region of the vein lumen (see Figure 13A) whereas the presence of a conical clot forces most of the blood flow throughout an annular region in between the clot and the vein wall (Figure 13B). Table 3 shows the values of the recirculation region volume, V_{rec}, calculated in each case. As a general trend, the extent of the flow recirculation region grows with increasing blood flow rate and clot volume. For a given flow rate and clot size, V_{rec} also depends on the particular geometry of the clots and it is remarkable that the annular and piece–like clots produce larger recirculation regions than the conical clots do. In the combo cases, one might expect the V_{rec} value to be roughly the sum of the recirculation volumes for the respective single clot cases. The C_S+P_S case under exercise conditions does not follow this rule as its V_{rec} = 0.70 cm^3 value is even smaller than the corresponding value for the P_S simulation (V_{rec} = 0.96 cm^3). Under exercise conditions, the presence of the downstream (conical) clot partially inhibits flow recirculation past the upstream (piece–like) clot. Note that under rest conditions, as the recirculation volume of the piece–like clot is much smaller (see Table 3), there is basically no interaction between the two clots in the $\mathrm{C_S}$+$\mathrm{P_S}$ case.

Case		$\mathrm{C_S}$	$\mathrm{A_S}$	$\mathrm{P_S}$	$\mathrm{C_L}$	$\mathrm{A_L}$	$\mathrm{P_L}$	$\mathrm{C_S+A_S}$	$\mathrm{C_S+P_S}$
Rest	$V_{rec}(\mathrm{cm}^3)$	0.15	0.29	0.24	0.31	0.91	1.54	0.48	0.38
	$\bar{t}_{in}(\mathrm{s})$	2.76	2.65	2.74	2.66	2.52	2.53	2.64	2.62
	$\bar{t}_{sta}(\mathrm{s})$	2.59	11.26	20.30	2.71	9.87	31.71	4.17	4.13
	$\overline{\mu}_{rec}/\overline{\mu}$	1.25	2.13	3.16	1.11	1.81	2.03	1.75	2.26
Exercise	$V_{rec}(\mathrm{cm}^3)$	0.20	1.01	0.96	0.74	2.04	2.64	1.16	0.70
	$\bar{t}_{in}(\mathrm{s})$	0.70	0.68	0.72	0.66	0.66	0.69	0.66	0.69
	$\bar{t}_{sta}(\mathrm{s})$	0.77	1.04	1.74	0.91	1.11	1.43	1.00	1.08
	$\overline{\mu}_{rec}/\overline{\mu}$	0.92	0.95	1.24	0.85	1.06	1.10	0.94	1.13

TABLE 3 Data on recirculation regions, characterized as the lumen volume with $U_z < 0$. The V_{rec} symbol denotes the recirculation volume, $\bar{t}_{in}$ is an estimate of the average time in which blood travels from the infrarenal inlet section to the suprarenal outlet section, and $\bar{t}_{sta}$ is an estimate of the average residence time of blood in the recirculation region. The $\bar{t}_{in}$ and $\bar{t}_{sta}$ times are calculated by numerical integration of a large number of trajectories of idealized (inert) particles being carried by the flow. In these calculations, particles were homogeneously seeded throughout the recirculation region ($\bar{t}_{sta}$) or the infrarenal inlet section ($\bar{t}_{in}$). The $\overline{\mu}$ and $\overline{\mu}_{rec}$ symbols denote the volume averaged viscosity values in the whole blood lumen and in the flow recirculation region, respectively.

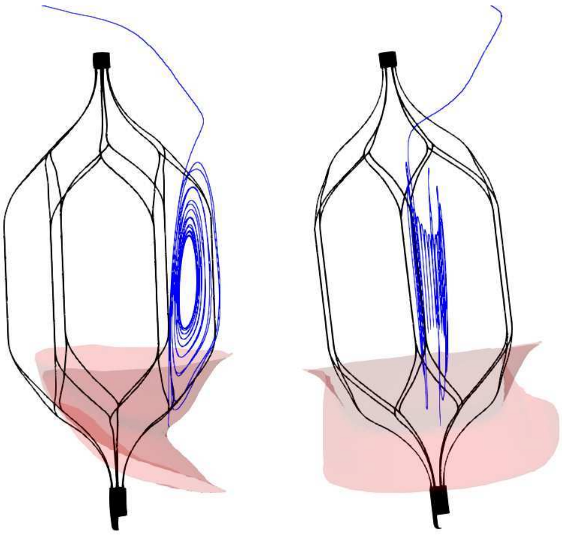

FIGURE 14 Two different views of an individual particle trajectory for the $\mathrm{P_L}$ case under rest conditions. The final integration time of the selected trajectory was $t_{sta} = 75.71$ s.

It has been stated in the literature on the subject that flow recirculation and stagnation regions become ideal environments for clot growth[18]. In this respect, a quantity more relevant than the size of the flow stagnation region is the residence time, $\bar{t}_{sta}$, that (on the average) blood will remain trapped within the wake region downstream of the clot[49]. The estimates of $\bar{t}_{sta}$ shown in Table 3 were obtained by numerical integration of a large number of trajectories throughout the recirculation region. Note that for steady state solutions each of such individual trajectories is also a flow streamline. The $\bar{t}_{in}$ reference quantity shown in Table 3, also obtained by numerical integration of many trajectories, can be interpreted as the average time in which an idealized, microscopic fluid parcel travels from the infrarenal inlet section to the suprarenal outlet section. As expected, $\bar{t}_{in}$ is roughly inversely proportional to the blood flow rate, V_{in}, and it is nearly independent of the clot geometries involved in each case. On the contrary, the $\bar{t}_{sta}$ values listed in Table 3 are strongly dependent not only on V_{in} but on the particular clot geometry as well. At the higher blood flow rate (exercise conditions), values of the $\bar{t}_{sta}/\bar{t}_{in}$ ratio are at most about two (in the $\mathrm{P_S}$ and $\mathrm{P_L}$ cases). Under rest conditions, we can see in Table 3 much larger $\bar{t}_{sta}$ values for the annular ($\mathrm{A_S}$, $\mathrm{A_L}$) and piece–like ($\mathrm{P_S}$, $\mathrm{P_L}$) clots, with a highest $\bar{t}_{sta}/\bar{t}_{in} = 12.5$ in the $\mathrm{P_L}$ case, whereas conical clots yield $\bar{t}_{sta}$ values still comparable to the corresponding $\bar{t}_{in}$ ones. Consequently, in the wake of the conical clot in Figure 13B flow streamlines spin at most two or three times along rather random looking paths, before they escape. For the $\mathrm{P_L}$ case in Figure 13A, we can see instead that streamlines tend to spin for much longer within the narrow recirculation region near the vein wall. To further illustrate this issue, Figure 14 shows the detail of an individual trajectory, viewed from two different angles, for the $\mathrm{P_L}$ case under rest conditions. The view angle in the lef plot of Figure 14 is similar to the one used in Figure 13 whereas the view angle in the right plot of Figure 14 was chosen to stress the fact that streamlines in the wake of this clot may spin many times, tracing unruffled, quasi–2D paths (i.e., each streamline spin is almost closed on a given plane, roughly normal to the view plane of the plot).

It seems also clear that, as a general rule, the higher is the blood viscosity in a given flow region the higher will be the risk of thrombogenesis in that region. Table 3 also includes calculated values of the ratio of the average blood viscosity within the recirculation region, $\overline{\mu}_{rec}$, to the corresponding average viscosity on the whole calculation domain, $\overline{\mu}$. For a given blood flow rate and clot size, the lowest and highest viscosity ratios are respectively observed for the conical and the piece–like clots. For a given clot geometry, the values of the viscosity ratio are always larger at the lowest blood flow rate (rest conditions); in fact, in exercise conditions $\overline{\mu}_{rec}$ exceeds $\overline{\mu}$ at most in 24% (in the $\mathrm{P_S}$ case). The combination of high residence times ($\bar{t}_{sta}$) and high blood viscosity ($\overline{\mu}_{rec}$) in the wake regions of the piece–like clots and, to a lesser extent, of the annular clots strongly hints to the possibility of a further clot growth under rest conditions (i.e., the conditions representative of what a real patient will experience most of the time).

3.5 | Flow unsteadiness and turbulence

Time–periodic solutions were obtained in the $\mathrm{C_S}$+$\mathrm{A_S}$, $\mathrm{P_L}$ and $\mathrm{C_L}$ cases under exercise conditions. As shown in the pressure time evolution plots of Figure 15, the oscillations in the $\mathrm{C_S}$+$\mathrm{A_S}$ (Fig.15A) and $\mathrm{C_L}$ (Fig.15C) cases display a very similar period of about 0.16 s whereas in the $\mathrm{P_L}$ case (Fig.15B) a much larger period of about 0.3 s is observed. The amplitudes of the oscillations in Figures 15A–C are by no means insignificant.

Inspection of the contours of the vertical velocity component, plotted in Figure 16 (A,B), helps to understand the nature of the flow oscillation in the $\mathrm{C_S}$+$\mathrm{A_S}$ case. Despite the symmetry of the conical clot both the blood flow distribution around it and the shape of the recirculation region in its wake are strongly asymmetric. The wake behind the conical clot bends to the left in the plane of Figure 16, that is, to the same side where the strongest flow jet in between the clot and the vein wall is observed. Note that the probe that collected the data plotted in Figure 15A was strategically placed in the shear layer region in between the strong blood jet and the conical clot wake. At some particular time instances, as illustrated in Figure 16A, the probe location lies within the flow stagnation region and lower p and negative U_z values were then recorded. The opposite situation, when higher p and positive U_z values were recorded, is illustrated in Figure 16B.

The appearance of the secondary peak in the time evolution plotted in Figure 15C, and the corresponding velocity phase diagram in Figure 15D, hint at the potential appearance of the period–doubling phenomenon (were the flow or geometry conditions somehow modified). In most dynamical systems period–doubling is a well established precursor of a subsequent transition to chaos[50]. It is therefore not surprising that, as shown in Figure 15E, significant levels of the so-called laminar kinetic energy, k_L, are found in the wake of the conical clot. Interestingly, the turbulence model predicts no real turbulence development in this case as the levels of turbulent kinetic energy, k_T, are maintained to zero (within the limits of numerical accuracy) in the whole calculation domain. The corresponding U_z contour plots in Figures 16(C,D) reveal that the physics underlying the oscillation in the $\mathrm{C_L}$ case is similar to that observed in Figure 16(A,B) for the $\mathrm{C_S}$+$\mathrm{A_S}$ case, i.e., the recirculation region behind the conical clot oscillates and keeps bending leftward. Note however that in Figures 16(C,D), contrary to what is observed in Figures 16(A,B), the strongest vertical motion is on the right side of the conical clot.

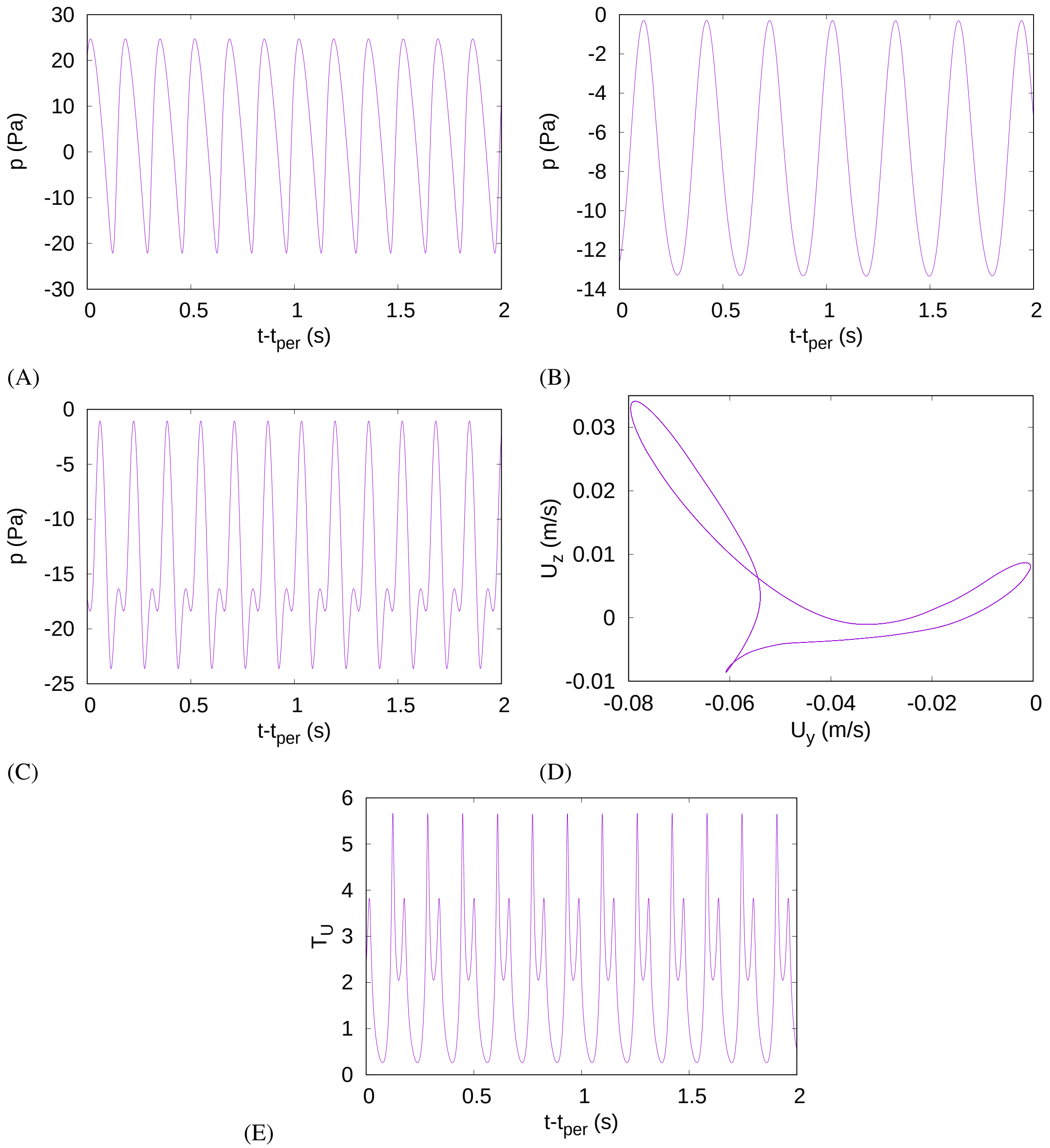

(A)

(B)

(C)

(D)

(E)

FIGURE 15 Time evolution of pressure (A-C) and turbulence intensity (E), as recorded at selected monitoring locations in the clot wake for the (A) $\mathrm{C_S}$+$\mathrm{A_S}$, (B) $\mathrm{P_L}$ and (C,E) $\mathrm{C_L}$ simulations under exercise conditions; see Eq. (8) for the definition of the turbulence intensity, T_U. Part (D) shows the U_z/U_y phase diagram corresponding to the same time interval and probe location as in (C). In parts (A-C) and (E) the t_{per} symbol in the axis of abscissas label denotes a reference value of the integration time when the flow oscillation was deemed to be already fully periodic.

Moreover, in the $\mathrm{C_L}$ case under exercise conditions we found that significant levels of k_L and ν_T where restricted to a small region downstream of the conical clot. That is, as the flow redeveloped downstream of the clot all signals of turbulence development vanished. As mentioned above, flow measurements by Leask et al.[17] and Harlal et al.[18] in experimental setups with similar conical clots but of a larger volume (1.5 cm^3) showed the existence of large regions of turbulent flow downstream of the obstacle. In order to find out whether a sufficiently large total clot volume would result in a more intense turbulence development we endeavored an additional combo simulation ($\mathrm{C_L}$+$\mathrm{P_L}$) having both the 1 cm^3 conical clot and the 1 cm^3 piece–like clot

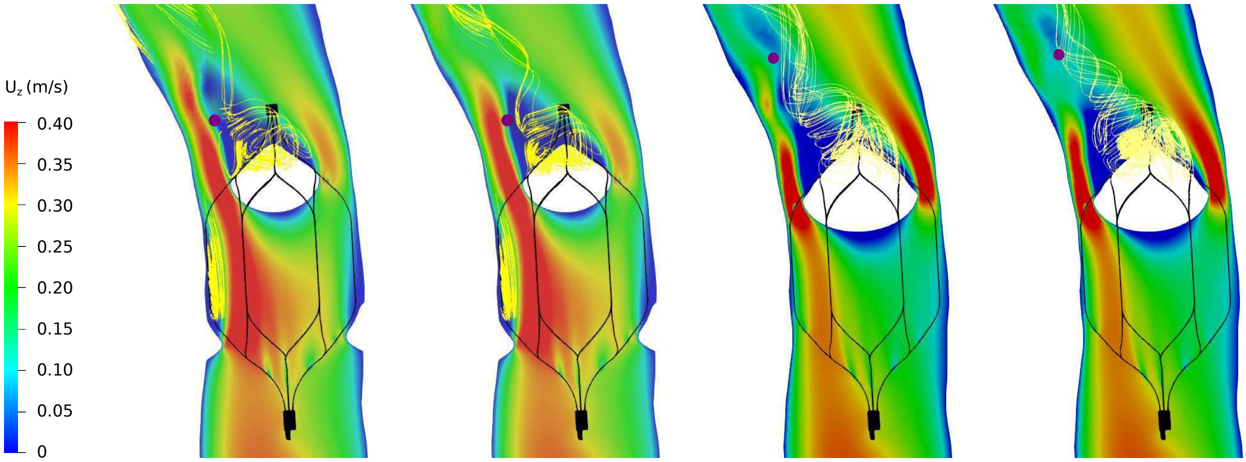

(A) (B) (C) (D)

FIGURE 16 Results for the (A, B) C_S+A_S case and (C, D) the C_L case under exercise conditions. Contour plots of the vertical velocity component, U_z, are shown at a selected plane slice at two time instants. Projections of a number of streamlines are also shown. The small purple circle denotes the location of the probe where data plotted in Figure 15 were recorded.

under exercise conditions. The computed recirculation volume was $V_{rec} = 1.51$ cm^3, less than the sum of the corresponding V_{rec} values obtained in the cases with either clot alone (0.74 and 2.64 cm^3 for the C_L and P_L cases, respectively; see Table 3). As can be seen in the time evolution of Figure 17A, a periodic solution was also obtained with significant levels of turbulent flow quantities. In this case, the calculated levels of turbulent kinetic energy, k_T, were significant although smaller, in about one order of magnitude, than the corresponding k_L values. Note that the frequency of the oscillation in Figure 17A is considerably higher than the frequency observed in the P_L case (Figure 15B) and also slightly higher than the frequencies observed in the C_S+A_S (Figure 15A) and C_L cases (Figure 15C, E).

The contours of turbulence intensity (T_U) shown in Figures 17C–E illustrate the fact that in the C_L+P_L simulation turbulence is mostly being generated in the wake of the conical clot, as well as in the region near the left side of the vein wall, downstream of the clot location. The 3D isosurface of the total fluctuation energy ($k_L + k_T$) in Figure 17B shows that, in contrast with the C_L case, turbulence does not decay but rather intensifies as the flow redevelops downstream of the clots. The additional blood flow through the right renal vein ($V_{ren} = 10$ cm^3/s) induces the appearance of turbulence near the right side of the vein wall. The subsequent flow inlet through the left renal vein ($V_{ren} = 10$ cm^3/s) pushes flow, having high levels of fluctuating kinetic energy, away from the left side of the wall.

4 | DISCUSSION AND CONCLUSIONS

In the present study we used CFD simulations to assess the effects on the blood flow of one or two clots attached to an OPTEASE® IVC filter. This filter features a double basket structure to enhance its clot capturing ability. It has therefore two independent clot capturing regions, a first one between the upstream basket and the vein wall and a second one within the umbrella–like central region of the downstream basket. In order to render the present simulations as realistic as possible we used a patient–specific vein wall geometry, we designed clot models whose shape was perfectly fitted to the filter struts and to the vein wall (see Figure 3) and we used a non–Newtonian model for blood viscosity. We found that the presence of either an upstream placed or a downstream placed clot considerably alters the WSS distribution on the vein wall. In the cases with a downstream clot the blood flow is channeled around the obstacle so that a ring–like vein wall area of high WSS values arises (see Figures 7B and E). As a consequence, the presence of a downstream clot increased the surface averaged wall shear stress ($\overline{\text{WSS}}$), especially at high blood flow rates (exercise conditions; see Figure 8). The upstream clots produced instead an extended wall region with low WSS behind the clot (see Figures 7C, D, F and G), indicative of very low values of the wall shear rate (typically, $\gamma_w < 10\,\text{s}^{-1}$). The existence of vein wall regions with low local γ_w and WSS values is also indicative of flow recirculation and stagnation phenomena that take place downstream of the clot. Moreover, the occurrence of low γ_w values has been

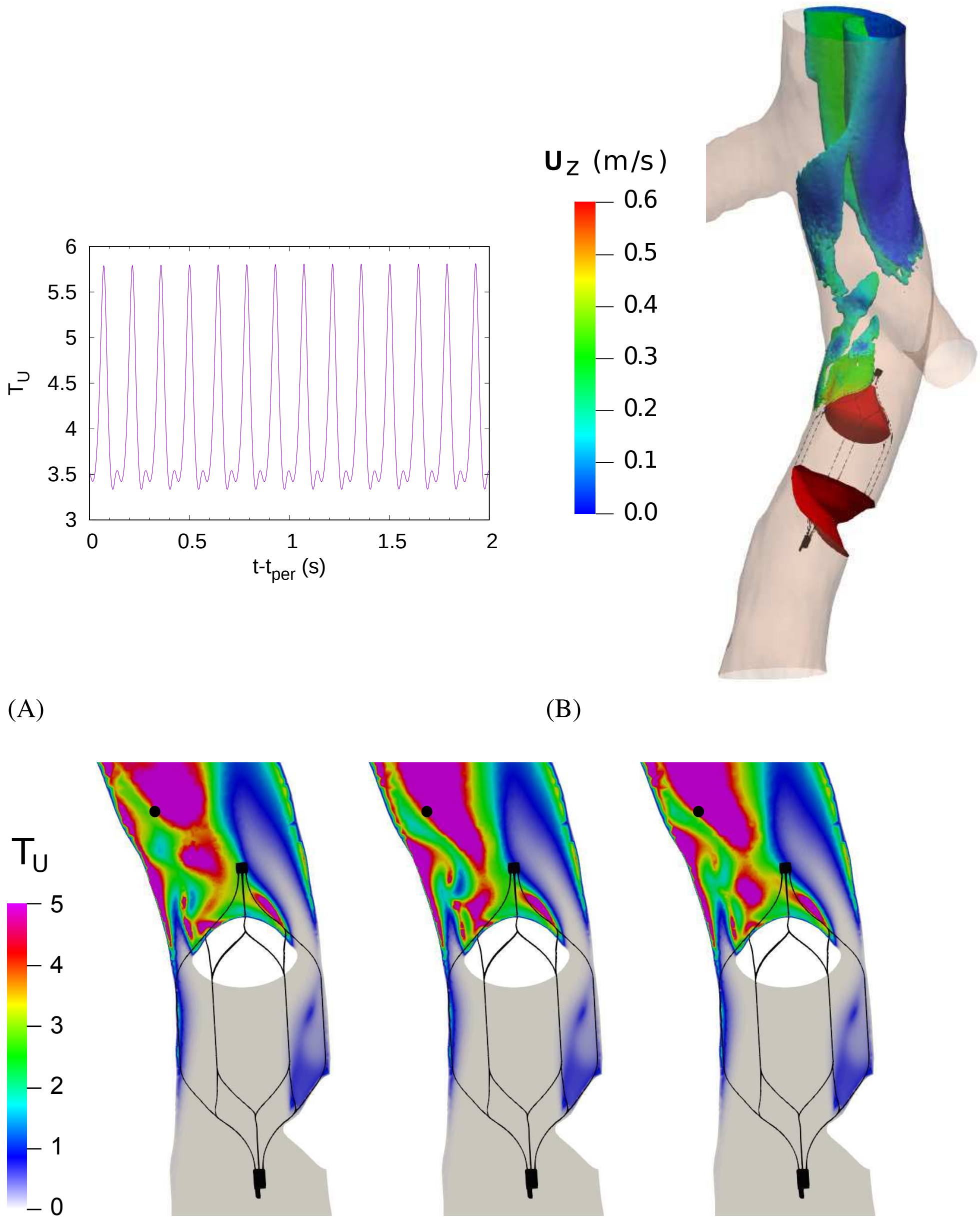

(A) (B)

(C) (D) (E)

FIGURE 17 Results for the additional C_L+P_L simulation under exercise conditions. (A) Time evolution of the turbulence intensity, T_U, as recorded at a point represented by the small black circle in parts (C–E). (B) Isosurface of $(k_L + k_T) = 10^{-4}$ m^{2}s^{-2}, colored according to the levels of the vertical component of velocity, U_z, at the particular instant with $t - t_{per} = 1.5$. (C–E) Contour plots of T_U at a selected plane slice and three time instants respectively close to minimum, intermediate and maximum values of T_U in part (A), namely $t - t_{per} = 1.14$ (C), 1.34 (D) and 1.5 (E). The plane of the slice used in parts (C–E) contains the probe point (denoted by a black circle) and is slightly behind (lower y) the parallel plane containing the filter axis.

reported to considerably enhance the adherence of erythrocytes to the vein wall, a physical mechanism which in turn might propitiate thombogenesis[51]. On the overall, the $\overline{\text{WSS}}$ values decreased in most of the cases in the presence of an upstream clot, or otherwise they just slightly increased.

The presence of clots also induces major changes in the pressure distribution within the blood lumen and along the vein wall. A considerable pressure raise is observed upstream from the clot whereas the wake region behind the clot is characterized by low pressure values. It is true that the increase in the total pressure drop along the simulated IVC section caused by the presence of the filter having clots attached (0.95 mm Hg at most, in the C_L case under exercise conditions) is modest from a clinical point of view. That is, the maximum increment in pressure drop would be a small percentage (about 1% at most) of the patient's blood tension and would therefore hardly represent a direct threat to the patient's health. Notwithstanding, a major issue resulting from high pressure drops around the clot (see Figure 10E) is in the magnitude of the drag force exerted by the blood flow on the clot (F_d). In comparison with the drag forces exerted on the filter, which are at most about 400 dyne under exercise conditions (see Figure 11), values as high as $F_d = 230$ and 2 200 dyne were predicted for the drag force on the clots under rest and exercise conditions, respectively (see Figure 12). Such large drag forces, which must be mostly counterbalanced by the reaction forces on the struts at the filter docking sites, might be one of the causes of often reported filter malfunctions such as protruding through the vein wall, strut fractures, tilting and even migration. We therefore wonder whether the health of a patient with an OPTEASE® filter implanted might be compromised when exercising, even if just for a short period of time.

The low pressure values in regions behind the clots are indicative of flow recirculation within these regions. Furthermore, regions with flow recirculation are usually associated with regions of flow stagnation, a physical situation which may well favor thrombogenesis[16,18]. The physics of the flow behind an upstream clot, partially attached to the vein wall, is somewhat analogous to that in the flow behind stenosed vein valves, a topic investigated by Bajd et al.[52] and Brass and Diamond[53]. These authors concluded that long residence times of flow in the poorly mixed eddy regions behind the valves provide favorable conditions for platelet aggregation and adherence. Consequently, a good indicator of the propensity for thrombogenesis in the clot wake would be, together with the presence of low γ_w and WSS, discussed above, the mean blood residence time ($\bar{t}_{sta}$; see Table 3). At the lower blood flow rate (rest conditions), high values of $\bar{t}_{sta}$ and mean blood viscosity in the recirculation region ($\overline{\mu}_{rec}$) were evident in the cases with an upstream clot (A_S, A_L, P_S, P_L) but they were not detected for conical clots (C_S, C_L). The increase in the blood flow rate from rest to exercise conditions results in a considerable enlargement of the flow recirculation region behind the upstream clots, especially for the small (0.5 cm^3) ones (A_S, P_S). Notwithstanding, in exercise conditions the calculated $\bar{t}_{sta}$ values are considerably reduced, being at most twice as big as are the corresponding values of $\bar{t}_{in}$ (the mean residence time of blood traveling from the infrarenal inlet section to the suprarenal outlet section). It is thus remarkable that for all the clot configurations investigated propensity for thrombogenesis is much reduced when the blood flow rate is sufficiently increased.

The notion that thrombogenesis ought to be avoided at any rate has led some authors to advise against the use of IVC filters having an upstream clot capturing area[16]. We think that such an idea might be somewhat unfair. First, it may be argued than nowadays practitioners tend to prescribe IVC filters not as an alternative but, in many instances, as a complement to the administration of anticoagulant drugs. Filters are suitable for PE patients that still suffer from deep vein thrombosis and that, as a consequence, will be still treated with anticoagulant therapy for a time period (by the end of which the IVC filter will have been probably retrieved). The presence of anticoagulant drugs in the blood flow would greatly reduce, if not completely eliminate, the risk of thrombogenesis around clots trapped by the IVC filter. Moreover, even in the absence of anticoagulant medication the dual clot trapping ability of the OPTEASE® filter (among other filter models) has also some merits compared to the single downstream trapping area strategy. Let as assume that an IVC filter has to trap two small (0.5 cm^3) clots. In the OPTEASE® filter, these two clots may concur and coalesce into the downstream basket or, alternatively, one of them might be trapped upstream from the filter. Let us compare for instance the results for the C_L and the $C_S + P_S$ simulations in the present study. In both cases the total clot volume is 1 cm^3. The former case, with a large conical downstream clot alone, features a considerably higher wall shear stress on the vein wall (see Figures 7 and 8). Thus, it may be argued that the single clot (downstream) trapping strategy, although favorable with respect to the dual trapping in some aspects (risk of thrombogenesis), may be less so considering the harm that high WSS levels might inflict on the vein wall tissue. Moreover, the results of the present study also suggest that a large downstream clot will have a higher tendency to induce flow instabilities and even turbulence, a phenomenon which some authors have also related to thrombogenesis[21,22]. In summary, it can be safely concluded that one big clot might well be more harmful than two small clots would be.

4.1 | Study limitations

Some limitations should be noted. The fully developed boundary conditions prescribed at the infrarenal inlet section might not be fully realistic. In some of the previous CFD studies on IVC filters[19,20,24] a vein geometry including the iliac veins region was considered. In the recent experimental study by Gallagher et al.[23], and its CFD counterpart by Craven et al.[24], two different inlet flow rates through the iliac veins were considered, namely $V_{in} = 1$ L/min for rest conditions (comparable to the present $V_{in} = 1.2$ L/min) and $V_{in} = 6$ L/min for exercise conditions (slightly higher than our $V_{in} = 4.8$ L/min). Under rest conditions, Craven et al. concluded that the flow was relatively simple, with flow from both iliacs merging to form a quasi-parabolic flow profile in the IVC with little secondary flow and mixing. However, these authors also reported that under exercise conditions the flow patterns were much more complex, as flow from the iliacs merged and interacted to form a pair of counter-rotating vortices with a high-velocity region in the center of the IVC lumen. The results of Craven et al. therefore suggest that while the present results are roughly independent of the prescribed inlet velocity distribution under rest conditions this might not be the case under exercise conditions.

The analysis of solid–fluid two–way interactions is beyond the scope of the present study. We analyzed how the presence of solid elements (IVC wall, clots and filter struts) modifies the flow, but not the other way round. We are aware that the assumption of rigid and immobile walls for all solid elements might be somewhat constraining. The elasticity of the blood vessel walls propitiates a self–regulatory mechanism against hypertension, when a high blood pressure episode is partly compensated by an increase in vessel diameter, which in turn keeps WSS and pressure levels at bay. As the present model does not account for the effects of wall elasticity, probably WSS values were slightly overestimated. The current assumption of clots being fitted to solid boundaries implies, in fact, a time evolution of the clot shape. That is, a clot might be trapped by the filter and subsequently change its shape and volume, progressively adapting to the solid surfaces that surround it. Our underlying assumption in this respect is that clot–shaping processes are very slow compared to the typical blood flow time–scales. The numerical values of the quantities presented in this study have to be understood as corresponding to particular *snapshots*, i.e., to selected shapes and volumes of the clots, *taken* along their time–evolution.

ACKNOWLEDGEMENT

Financial support for the current research was granted by Universitat Rovira i Virgili, project number 2018PFR-URV-B2-29.

References

1. Shiraev TP, Omari A, Rushworth RL. Trends in pulmonary embolism morbidity and mortality in Australia. *Thrombosis Research* 2013; 132: 19–25. doi: 10.1016/j.thromres.2013.04.032
2. Keller K, Hobohm L, Ebner M, et al. Trends in thrombolytic treatment and outcomes of acute pulmonary embolism in Germany. *European Heart Journal* 2019; 0: 1–8. doi: 10.1093/eurheartj/ehz236
3. Kempny A, McCabe C, Dimopoulos K, et al. Incidence, mortality and bleeding rates associated with pulmonary embolism in England between 1997 and 2015. *International Journal of Cardiology* 2019; 277: 229–234. doi: 10.1016/j.ijcard.2018.10.001
4. Benjamin EJ, Muntner P, Alonso A, Bittencourt MS, Callaway CW, Carson AP. Heart Disease and Stroke Statistics–2019 Update. A Report From the American Heart Association. *Circulation* 2019; 139: e56–e528. doi: 10.1161/CIR.0000000000000659
5. Kearon C, Akl EA, Ornelas J, et al. Antithrombotic Therapy for VTE Disease. CHEST Guideline and Expert Panel Report. *CHEST* 2016; 149(2): 315–352. doi: 10.1016/j.chest.2015.11.026
6. Yunus TE, Tariq N, Callahan RE, et al. Changes in inferior vena cava filter placement over the past decade at a large community-based academic health center. *J Vasc Surg* 2008; 47(1): 157–165. doi: 10.1016/j.jvs.2007.08.057
7. Lenchus JD, Biehl M, Cabrera J, Gallo de Moraes A, Dezfulian C. In-hospital Management and Follow-Up Treatment of Venous Thromboembolism: Focus on New and Emerging Treatments. *J Intensive Care Med* 2016. doi: 10.1177/0885066616648265
8. Zhang F, Li D, Liu J, Zhang H. The Vena Tech LP Permanent Caval Filter: Effectiveness and Safety in the Clinical Setting in Three Chinese Medical Centers. *Thromb Res* 2015; 136: 40–44. doi: 10.1016/j.thromres.2015.04.015
9. Decousus H, Leizorovicz A, Parent F, et al. A clinical trial of vena cava filters in the prevention of pulmonary embolism in patients with proximal deep–vein thrombosis. *New Engl J Med* 1998; 338(7): 409–415.

10. Haddadian B, Shaikh F, Dielmami-Hani M, Shalev Y. Sudden Cardiac Death Caused by Migration of a TrapEase Inferior Vena Cava Filter: Case Report and Review of the Literature. *Clin. Cardiol.* 2008; 31: 84–87. doi: 10.1002/clc.20156
11. Grewal S, Chamarthy MR, Kalva SP. Complications of inferior vena cava filters. *Cardiovasc Diagn Ther* 2016; 6: 632–641. doi: 10.21037/cdt.2016.09.08
12. López JM, Fortuny G, Puigjaner D, Herrero J, Marimon F. A comparative CFD study of four inferior vena cava filters. *Int J Numer Method Biomed Eng* 2018; 34(7): e2990. doi: 10.1002/cnm.2990
13. Cordis . OPTEASE® Retrievable Vena Cava Filter. https://www.cordis.com/en_us/endovascular/intervene/vena-cava-filters/optease-retrievable-vena-cava-filter.html; 2019. Accessed 30-Oct-2019.
14. U.S. Food and Drug Administration . Manufacturer and User Facility Device Experience (MAUDE) database. https://www.accessdata.fda.gov/scripts/cdrh/cfdocs/cfmaude/search.cfm; 2020. Accessed 09-Jan-2020.
15. Stewart SFC, Robinson RA, Nelson RA, Malinauskas RA. Effects of Thrombosed Vena Cava Filters on Blood Flow: Flow Visualization and Numerical Modeling. *Ann Biomed Eng* 2008; 36(11): 1764–1781. doi: 10.1007/s10439-008-9560-6
16. Singer MA, Henshaw WD, Wang SL. Computational Modeling of Blood Flow in the TrapEase Inferior Vena Cava Filter. *J. Vasc. Interv. Radiol.* 2009; 20(6): 799–805.
17. Leask R, Wayne Johnston K, Ojha M. Hemodynamic Effects of Clot Entrapment in the TrapEase Inferior Vena Cava Filter. *J Vasc Interv Radiol* 2004; 15: 485–90. doi: 10.1097/01.RVI.0000124941.58200.85
18. Harlal A, Ojha M, Johnston KW. Vena cava filter performance based on hemodynamics and reported thrombosis and pulmonary embolism patterns. *J Vasc Interv Radiol* 2007; 18: 103–115. doi: 10.1016/j.jvir.2006.10.020
19. Rahbar E, Mori D, Moore JE. Three-dimensional analysis of flow disturbances caused by clots in inferior vena cava filters. *J Vasc Interv Radiol* 2011; 22: 835–842. doi: 10.1016/j.jvir.2010.12.024
20. Ren Z, Wang SL, Singer MA. Modeling hemodynamics in an unoccluded and partially occluded inferior vena cava under rest and exercise conditions. *Med. Biol. Eng. Comput.* 2012; 50: 277–287. doi: 10.1007/s11517-012-0867-y
21. Stein PD, Sabbah HN. Measured turbulence and its effect on thrombus formation. *Circulation Research* 1974; 35: 608–614.
22. Olgun A, Akman S, Erbil MK. The role of RBC destruction in vascularregions with high turbulence on atherosclerosis. *Medical Hypotheses* 2004; 63: 283–284. doi: 10.1016/j.mehy.2004.02.034
23. Gallagher MB, Aycock K, Craven BA, Manning K. Steady Flow in a Patient-Averaged Inferior Vena Cava–Part I: Particle Image Velocimetry Measurements at Rest and Exercise Conditions. *Cardiovascular Engineering and Technology* 2018; 9(4): 641–653. doi: 10.1007/s13239-018-00390-2
24. Craven BA, Aycock K, Manning K. Steady Flow in a Patient-Averaged Inferior Vena Cava—Part II: Computational Fluid Dynamics Verification and Validation. *Cardiovascular Engineering and Technology* 2018; 9: 654——673. doi: 10.1007/s13239-018-00392-0
25. Aycock KI, Campbell RL, Manning KB, et al. A Computational Method for Predicting Inferior Vena Cava Filter Performance on a Patient–Specific Basis. *J Biomech Eng-T ASME* 2014; 136(8). doi: 10.1115/1.4027612
26. Aycock KI, Campbell RL, Lynch FC, Manning KB, Craven BA. The Importance of Hemorheology and Patient Anatomy on the Hemodynamics in the Inferior Vena Cava. *Ann Biomed Eng* 2016; 44(12): 3568–3582. doi: 10.1007/s10439-016-1663-x
27. Wang SL, Timmermans HA, Kaufman JA. Estimation of Trapped Thrombus Volumes in Retrievable Inferior Vena Cava Filters: A Visual Scale. *J Vasc Interv Radiol* 2007; 18: 273–276. doi: 10.1016/j.jvir.2006.12.732
28. Teo TKB, Angle JF, Shipp JI, et al. Incidence and Management of Inferior Vena Cava Filter Thrombus Detected at Time of Filter Retrieval. *J Vasc Interv Radiol* 2011; 22: 1514–1520. doi: 10.1016/j.jvir.2011.08.006
29. McCowan TC, Ferris EJ, Carver DK. Inferior Vena Caval Filter Thrombi: Evaluation with Intravascular US. *Radiology* 1990; 177: 783–788.

30. Nutting C, Coldwell D. Use of a TrapEase Device as a Temporary Caval Filter. *J Vasc Interv Radiol* 2001; 12: 991–993.
31. The OpenFOAM Foundation . OpenFOAM. http://openfoam.org/; 2019. Accessed 30-Oct-2019.
32. Bird RB, Amstrong RC, Hassager O. *Dynamics of Polimeric Liquids*. New York: John Wiley & Sons. second ed. 1987.
33. Fortuny G, Herrero J, Puigjaner D, et al. Effect of anticoagulant treatment in deep vein thrombosis: a patient–specific computational fluid dynamics study. *J Biomech* 2015; 48: 2047–2053. doi: 10.1016/j.jbiomech.2015.03.026
34. Gijsen F, Allanic E, Vosse v. dF, Janssen J. The in#uence of the non-Newtonian properties of blood on the #ow in large arteries: unsteady #ow in a 903 curved tube. *Journal of Biomechanics* 1999; 32: 705–713.
35. Johnston BM, Johnston PR, Corney S, Kilpatrick D. Non–Newtonian blood flow in human right coronary arteries: steady state simulations. *J Biomech* 2004; 37: 709–720. doi: 10.1016/j.jbiomech.2003.09.016
36. Chen J, Lu XY, Wang W. Non–Newtonian effects of blood flow on hemodynamics in distal vascular graft anastomoses. *Journal of Biomechanics* 2006; 39: 1983–1995.
37. Soulis JV, Giannoglou GD, Chatzizisis YS, Seralidou KV, Parcharidis GE, Louridas GE. Non–Newtonian models for molecular viscosity and wall shear stress in a 3D reconstructed human left coronary artery. *Medical Engineering & Physics* 2008; 30: 9–19. doi: 10.1016/j.medengphy.2007.02.001
38. Razavi A, Shirani E, Sadeghi MR. Numerical simulation of blood pulsatile flow in a stenosed carotid artery using different rheological models. *J Biomech* 2011; 44: 2021–2030. doi: 10.1016/j.jbiomech.2011.04.023
39. Karimi S, Dabagh M, Vasava P, Dadvar M, Dabir B, Jalali P. Effect of rheological models on the hemodynamics within human aorta: CFD study on CT image–based geometry. *Journal of Non-Newtonian Fluid Mechanics* 2014; 207(0): 42–52.
40. Trias M, Arbona A, Massó J, Miñano B, Bona C. FDA's Nozzle Numerical Simulation Challenge: Non- Newtonian Fluid Effects and Blood Damage. *PLoS ONE* 2014; 9(3): e92638.
41. Al-Azawy MG, Turan A, Revell A. Investigating the impact of non–Newtonian blood models within a heart pump. *International Journal for Numerical Methods in Biomedical Engineering* 2017; 33(1): e02780.
42. Cheng AL, Pahlevan NM, Rinderknecht DG, Wood JC. Experimental Investigation of the Effect of Non–Newtonian Behavior of Blood Flow in the Fontan Circulation. *Eur J Mech B Fluids* 2018; 68: 184–192.
43. Walters DK, Cokljat D. A three-equation Eddy-viscosity model for Reynolds-averaged Navier-Stokes simulations of transitional flow. *Journal of Fluids Engineering* 2008; 130: 121401–1–121401–14. doi: 10.1115/1.2979230
44. Kitware . Paraview. http://www.paraview.org; 2019. Accessed 30-Oct-2019.
45. Kroll MH, Hellums JD, McIntire LV, Schafer AI, Moake JL. Platelets and Shear Stress. *Blood* 1996; 88(5): 1525–1541.
46. Turitto VT, Hall CL. Mechanical Factors Affecting Hemostasis and Thombosis. *Thrombosis Research* 1998; 92: S25–S31.
47. Hathcock JJ. Flow Effects on Coagulation and Thrombosis. *Arterioescler Thromb Vasc Biol* 2006; 26: 456–461.
48. Pfisterer L, König G, Hecker M, Korff T. Pathogenesis of varicose veins – lessons from biomechanics. *Vasa* 2014; 43: 88–99.
49. Menichini C, Cheng Z, Gibbs RGB, Xu XY. Predicting false lumen thrombosis in patient-specific models of aortic dissection. *J. R. Soc. Interface* 2016; 13: 20160759. doi: 10.1098/rsif.2016.0759
50. Seydel R. *Practical bifurcations and stability analysis*. London: Springer. third ed. 2010.
51. Goel MS, Diamond SL. Adhesion of normal erythrocytes at depressed venous shear rates to activated neutrophils, activated platelets, and fibrin polymerized from plasma. *Blood* 2002; 100(10): 3797–3803. doi: 10.1182/blood-2002-03-0712
52. Bajd F, Vidmar J, Fabjan A, et al. Impact of altered venous hemodynamic conditions on the formation of platelet layers in thromboemboli. *Thrombosis Research* 2012; 129: 158–163. doi: 10.1016/j.thromres.2011.09.007

53. Brass LF, Diamond SL. Transport physics and biorheology in the setting of hemostasis and thrombosis. *J Thromb Haemost* 2016; 14: 906–917.

How to cite this article: López J M, Fortuny G, Puigjaner D, and Herrero J ( ), Hemodynamic effects of different clot shapes as held by a vena cava filter, *Int J Numer Meth Biomed Engng.*, .